Part I

Building blocks of quantum communication networks

Chapter 2

SOURCES AND DETECTORS

This chapter includes the work published as:

[1] Volkan Gurses, Samantha I. Davis, Esme Knabe, Raju Valivarthi, Maria Spiropulu, and Ali Hajimiri. "A compact silicon photonic quantum coherent receiver with deterministic phase control." In: CLEO: Applications and Technology. Optica Publishing Group. 2023, AM4N–4.

[1] Volkan Gurses, Debjit Sarkar, Samantha Davis, and Ali Hajimiri. "An integrated photonic-electronic quantum coherent receiver for sub-shot-noise-limited optical links." In: Optical Fiber Communication Conference. Optica Publishing Group. 2024, Tu2C–1.

2.1 Sources

A defining feature of quantum networks is their ability to distribute quantum information between distant nodes while preserving quantum coherence. Photons are the primary carriers of quantum information between nodes in a quantum network due to their ability to propagate over long distances in optical fiber or free space with relatively low decoherence. Quantum networks require reliable sources of indistinguishable photons for key network operations such as quantum interference. A standard approach to generating photons suitable for quantum networking is to use the strong light-matter coupling offered by solid-state bulk nonlinearities. In a bulk nonlinearity, the optical response of the nonlinear medium to a pump field is described by the polarization vector $\vec{P} = \vec{P}^{\mathrm{L}} + \vec{P}^{\mathrm{NL}}$, where $P_i^{\mathrm{L}} = \varepsilon_0 \sum \chi_{ij}^{(1)} E_j$ is the linear term containing the first order susceptibility, $\chi^{(1)}$, and $\vec{P}^{\mathrm{NL}}$ is the nonlinear term containing contributions from higher-order susceptibilities, $\chi^{(n)}$ [1]. Pairs of single photons can be probabilistically emitted from nonlinear materials via laser-driven second-order ($\chi^{(2)}$) and third-order ($\chi^{(3)}$) processes such as spontaneous parametric down-conversion and spontaneous four-wave mixing, respectively. Photon pair generation provides versatile sources of entanglement and heralded single photons with high purity, bandwidth, and tunability.

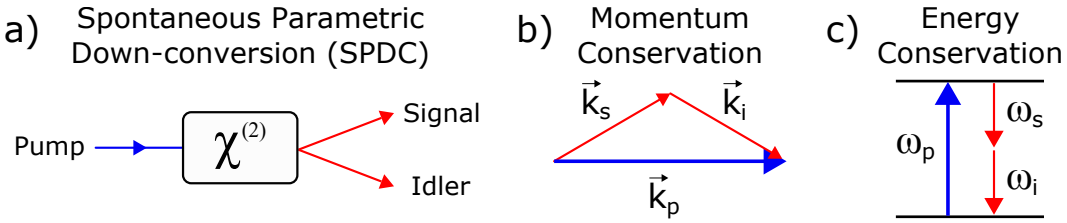

Figure 2.1: Spontaneous parametric down-conversion (SPDC). a) A pump photon is spontaneously downconverted into a pair of signal and idler photons by a $\chi^{(2)}$ bulk optical nonlinearity. The pump, signal and idler photons satisfy phase matching conditions, namely b) momentum conservation ($\vec{k}_p = \vec{k}_s + \vec{k}_i$) and c) energy conservation ($\hbar\omega_p = \hbar\omega_s + \hbar\omega_i$).

Spontaneous Parametric Down Conversion

Spontaneous parametric down-conversion (SPDC) is a three-wave mixing process involving the interaction of a pump, signal, and idler photon in a medium with a leading order $\chi^{(2)}$ bulk nonlinearity. A single pump photon with frequency ω_1 is spontaneously converted into a pair of lower-energy signal and idler photons with frequency ω_2 and ω_3, respectively (see Fig. 2.1). The SPDC process obeys energy and momentum conservation rules, also referred to as the phase-matching conditions,

$$\hbar\omega_3 = \hbar\omega_1 + \hbar\omega_2, \tag{2.1}$$

$$\Delta\vec{k} = \vec{k}_3 - \vec{k}_1 - \vec{k}_2 = 0, \tag{2.2}$$

where $\vec{k}_i$ represents the wave vector with magnitude $k_i = n(\omega_i)\omega_i/c$ and $n_i(\omega_i)$ is the index of refraction. The process is described by the interaction Hamiltonian,

$$\hat{H}_{\text{int}} = i\hbar\kappa\left(\hat{a}_1^\dagger\hat{a}_2^\dagger\hat{a}_3 + \hat{a}_1\hat{a}_2\hat{a}_3^\dagger\right) \tag{2.3}$$

where $\kappa \propto \chi^{(2)}L$ is a constant that depends on strength of the nonlinearity ($\chi^{(2)}$) and interaction length (L), and $\hat{a}$, $\hat{a}^\dagger$ are the bosonic ladder operators [2]. In Eq. 2.3, the first term corresponds to the creation of signal ($\hat{a}_1^\dagger$) and idler ($\hat{a}_2^\dagger$) photons by the annihilation of a pump photon ($\hat{a}_3$). The second term accounts for time reverse of the process, sum frequency generation (SFG) or second harmonic generation (SHG) for $\omega_1 = \omega_2$, where two photons ($\hat{a}_1$, $\hat{a}_2$) are converted into a photon ($\hat{a}_3^\dagger$) of higher energy. The quantum state at the output of the SPDC process is,

$$|\psi(t)\rangle = \exp\left(\frac{1}{i\hbar}\int_0^t \hat{H}_{\text{int}}(t')dt'\right)|0\rangle \approx \left(1 + \frac{1}{i\hbar}\int_0^t \hat{H}_{\text{int}}(t')dt' + \cdots\right)|0\rangle\,, \tag{2.4}$$

where $|0\rangle$ is the initial vacuum state. In Eq. 2.4, $|\psi(t)\rangle$ corresponds to a single mode squeezed vacuum state (SMSV) in the degenerate case ($\omega_1 = \omega_2$) and a two-mode squeezed vacuum (TMSV) state in the nondegenerate case ($\omega_1 \neq \omega_2$) of signal and idler photons. The right hand side of Eq. 2.4 is the perturbative expansion of the time evolution operator to leading order in κ in the non-depleted pump approximation, where κ is typically very small with most of the pump photons unconverted. The leading order (two-photon) component of $|\psi(t)\rangle$ is,

$$|\psi\rangle \propto \kappa \int_0^\infty \int_0^\infty f(\omega_1, \omega_2)\hat{a}_1^\dagger(\omega_1)\hat{a}_2^\dagger(\omega_2)d\omega_1 d\omega_2 \, |0\rangle_1 \, |0\rangle_2 \tag{2.5}$$

where L is the interaction length and $f(\omega_1, \omega_2)$ is the joint spectral amplitude (JSA). The JSA accounts for the spectral profile of the pump and phase matching condition,

$$f(\omega_1, \omega_2) = \psi_{\mathrm{p}}(\omega_1, \omega_2) \cdot \psi_{\mathrm{ph}}(\omega_1, \omega_2), \tag{2.6}$$

where $\psi_{\mathrm{p}}(\omega_1, \omega_2)$ is the pump envelope and $\psi_{\mathrm{ph}}(\omega_1, \omega_2)$ is the phase matching envelope. The joint spectral intensity (JSI), $|f(\omega_1, \omega_2)|^2$, is the probability distribution of signal and idler frequencies.

Phase matching Efficient generation of photon pairs requires careful design of SPDC sources to achieve the phase matching conditions as much as possible [1, 3]. For instance, the phase matching condition $\Delta k = 0$ demands appropriate refractive indices $n(\omega_3) > n(\omega_1)$ and $n(\omega_2)$, which cannot be fulfilled with centrosymmetric materials. The phase-matching condition can be satisfied naturally in birefringent materials, such as barium borate (BBO), potassium titanyl phosphate (KTP), and lithium niobate (LN), with different indices of refraction depending on the polarization and direction of propagation of the electric field for a given frequency. Phase matching can be achieved by tuning the angle of the pump field relative to the optic axis, resulting in different phase-matching configurations depending on the geometry [4]. Photon pairs can be emitted collinearly or non-collinearly depending on the type of phase-matching configuration (see Fig 2.1). In type-I SPDC, the signal and idler photons have the same polarization, which is orthogonal to the pump polarization, whereas in type-II SPDC, the signal and idler photons have orthogonal polarizations.

In type-0 SPDC, the pump, signal, and idler photons share the same polarization state; however, inherent material dispersion often prevents natural phase matching due to mismatched phase velocities of the interacting waves. Quasi-phase matching

can be achieved by periodic poling, where the sign of the nonlinear susceptibility tensor of the nonlinear crystal is spatially modulated at regular intervals, known as the poling period [5, 6]. A common technique is electric field poling, where a strong electric field is applied in a controlled pattern to induce periodic ferroelectric domain reversals. The periodic inversion compensates for the phase mismatch by effectively resetting the relative phase between the pump and generated photons at each poling period, thereby sustaining constructive interference over extended interaction lengths. The poling period is precisely engineered based on the wavelengths of the pump, signal, and idler photons, as well as the material's refractive indices, to satisfy the quasi-phase matching condition,

$$\Delta k = k_3 - k_1 - k_2 - 2\pi m/\Lambda, \tag{2.7}$$

where m is an integer and Λ is the poling period. Materials commonly subjected to periodic poling include LN and KTP due to their robust nonlinear properties and amenability to domain inversion.

Early demonstrations of photon-pair generation via type-I SPDC were crucial for fundamental tests of nonlocality [7] and two-photon interference [8]. Subsequent refinements in crystal growth, pump laser design, and alignment precision led to the development of sources with higher brightness and narrow bandwidths for practical implementations, with extensive investigation into type-II SPDC sources due to their intrinsically high-contrast polarization entanglement and convenient post-selection methods for measuring polarization correlations [4]. These advances, along with improvements in crystal purity, pump stability, and collection optics, fueled applications in entanglement-based quantum communication, culminating in demonstrations of entanglement distribution over fiber networks exceeding 10 km [9, 10] and paved the way for more complex multi-photon entanglement experiments [11]. In parallel, the advent of quasi-phase matching in periodically poled lithium niobate (PPLN) and potassium titanyl phosphate (PPKTP) led to a wide adoption of type-0 SPDC sources [10, 12], enabling higher nonlinear conversion efficiencies, flexible wavelength control, and compact waveguide implementations critical for integrated quantum networking architectures [5, 6].

Spectral Purity A typical joint spectral intensity for a type-II SPDC process is shown in Fig. 2.2, illustrating the broadband spectral correlations of photon pairs emitted by SPDC. Type-II SPDC exhibits narrower bandwidths than type-0 or type-I SPDC because orthogonal polarizations impose stricter phase matching constraints

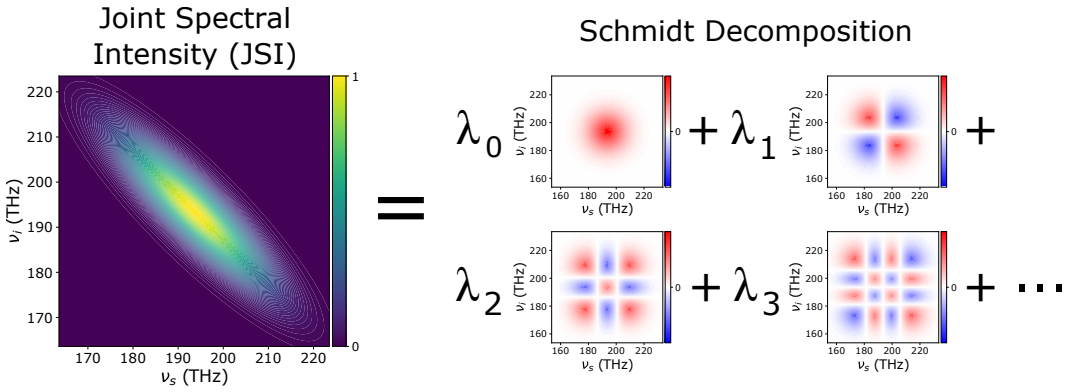

Figure 2.2: A typical joint spectral intensity for type-II SPDC for a pump photon at 775 nm, corresponding to signal and idler photons at telecom wavelengths centered at 1550 nm. By taking the singular value decomposition, the JSI can be decomposed into Schmidt modes (plotted) and associated eigenvalues $\{\lambda_n\}$, where λ_n^2 is the probability of occupying the nth mode.

[4, 13]. The degree of spectral entanglement can be characterized by the Schmidt decomposition of the two-photon state,

$$|\psi\rangle = \sum_j \sqrt{\lambda_j}\, |j\rangle_1 \, |j\rangle_2 \tag{2.8}$$

where $|\lambda\rangle_j$ are the Schmidt coefficients with $\sum_j \lambda_j = 1$ and $|j\rangle_1, |j\rangle_2$ are orthonormal states of the signal and idler modes, respectively. The Schmidt decomposition can be obtained by performing a singular value decomposition of the JSI (see Fig. 2.1e). The spectral purity of the photon pairs is quantified by the Schmidt number, $K = 1/\sum_j \lambda_j^2$, which is the effective number of occupied eignemodes. The Schmidt number is related to the purity $P = 1/K$ of the source, where $K = 1$ corresponds to signal and idler photons in a single spectral mode [14].

In practical networking implementations, bright and spectrally pure sources of photon pairs are needed for high-fidelity generation of single photons and entangled states such as Bell states. Spectral filtering is commonly employed to effectively isolate a single spectral mode and reduce multimode contributions. However, for high degrees of spectral correlations, filtering will block the majority of generated photon pairs, resulting in substantial photon loss and restricted pair production rates [15]. Instead of filtering, spectral engineering techniques [16, 17, 18, 19, 20, 21] can be employed to engineer the joint spectrum of the source. For example, in cavity-enhanced sources, optical cavities are used to enforce specific resonant frequencies, thereby selectively enhancing the generation of photon pairs within a

narrow spectral range and promoting single-mode operation [22]. Alternatively, multimode sources can be used for spectrally multiplexing to achieve high-rate photon pair production and entanglement distribution. Fiber-coupled, broadband type-0 SPDC sources at telecom wavelengths can be interfaced with commercial division wave demultiplexers to distribute photon pairs over many channels in a network [23]. Combining spectral engineering and multiplexing techniques can enable high-rate sources of indistinguishable photons required for entanglement-based protocols over long distances in advanced quantum networks.

2.2 Encoding quantum information

Photons can be used as carriers of quantum information in a number of degrees of freedom (DOFs), in both discrete variable and continuous variable encodings of quantum information.

Discrete variables

For discrete variable encodings of qubits, commonly used DOFs include polarization, time-energy, and orbital angular momentum, and time-of-arrival. Polarization encoding is among the most widely used, where horizontal and vertical polarization states define the computational basis. Polarization correlations of photon pairs, e.g., from type-II SPDC, are exploited to generate entangled states by taking advantage of the orthogonally polarized photon pairs emitted into distinguishable spatial modes. Energy-time encodings exploit the strong frequency correlations and time-energy uncertainty intrinsic to SPDC, where the emission time of an idler photon is uncertain but strongly correlated with the signal photon [24]. Orbital angular momentum (OAM) encodings use spatial modes carrying quantized angular momentum, allowing access to high-dimensional Hilbert spaces and offering greater information capacity per photon [25].

An essential feature of quantum networks is the ability to distribute entanglement across many distributed nodes over nominally long distances. An attractive approach is to leverage the commercial optical fiber infrastructure already developed at telecom wavelengths for the deployment of large-scale quantum networks. For this approach, qubits encoded in the time-of-arrival states (early $|e\rangle$ or late $|\ell\rangle$) of individual photons, or "time-bin qubits," at telecom-band wavelengths are preferred due to their ease of generation, low-loss propagation, and robustness to phase noise and polarization drift in over long-distances in optical fibers [26].

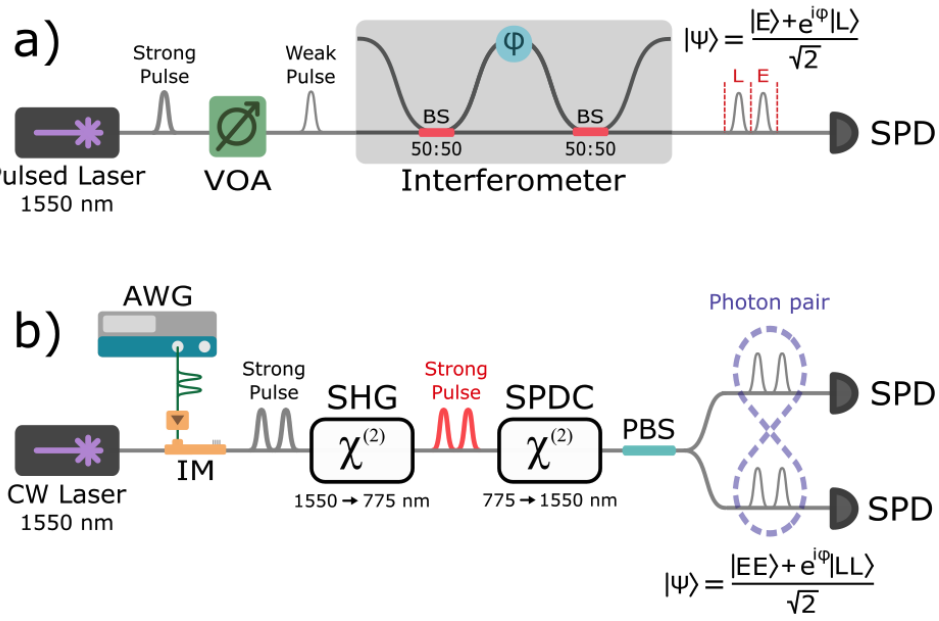

Figure 2.3: Generation of time-bin qubits at telecom wavelengths with commercially available fiber-optic components. a) Strong pulses of coherent light from a mode-locked laser are attenuated down to the single photon level by a variable optical attenuator (VOA). The weak pulses are inserted into an path-length-imbalanced interferometer, which defines early (E) and late (L) time-bins corresponding a photon passing through the short and long path, respectively. A photon at the output of the interferometer is in a coherent superposition of early and late time-of-arrival states. b) Early and late pulses are carved out from a continuous wave (CW) laser by an intensity modulator (IM), which is programmed by an arbitrary waveform generator (AWG) to define the early and late time-bins. The strong pulses are frequency-doubled by a second harmonic generator (SHG) to serve as pump light for spontaneous parametric down-conversion (SPDC), which produces pairs of single photons at telecom wavelength in an approximate Bell state. Quantum states are post-selected by a single-photon detector (SPD) that measures its time-of-arrival state.

Time-bin qubits Time-bin qubits are generated by preparing single photons in a coherent superposition of pulses separated by a fixed time delay, defining "early" and "late" temporal modes. By setting the temporal separation of the pulses much shorter than the coherence time of the channel, the relative phase between the two time-bins remains stable over long-distance fiber transmission, preserving quantum coherence. The computational (Z) basis ($|e\rangle$, $|l\rangle$) is defined by preparing a single photon in an early ("e") or late ("l") time bin. A qubit in the X basis, $|\pm\rangle = \frac{1}{\sqrt{2}}(|e\rangle \pm |l\rangle)$, or Y basis, $|\pm\rangle = \frac{1}{\sqrt{2}}(|e\rangle \pm i\,|l\rangle)$, can be prepared by sending a single photon to a path-imbalanced interferometer, where the time delay between the short and long paths inside the interferometer sets the temporal separation of the time bins (see Fig. 2.3a). The state of a photon at one of the outputs of the interferometers is described by $(|e\rangle + e^{i\phi}\,|l\rangle)/\sqrt{2}$, where ϕ is controlled by the interferometric phase shifter.

Deterministic and on-demand generation of pure single photons is a ongoing experimental challenge [27]. Due to ease of generation, a common approach is to approximate a single photons as a weak coherent state,

$$|\alpha\rangle = e^{-|\alpha|^2/2}\sum_{n=0}^{\infty}\frac{\alpha^n}{\sqrt{n!}}\,|n\rangle = e^{-|\alpha|^2/2}(|0\rangle + \alpha\,|1\rangle + O(|\alpha|^2)), \qquad |\alpha|^2 \ll 1, \tag{2.9}$$

where the subscript e (l) denotes the early (late) temporal mode, $|n\rangle$ is the photon number state of n photons, and $|\alpha|^2$ is the mean photon number. Single photons in confined temporal modes can be prepared by attenuating a series of laser pulses down the single-photon level. Each pulse defines a time bin within its clock cycle, which is set by the repetition rate of the laser. The preparation of a photon in the early or late time-bin is performed by changing the timing of the pulse within its clock cycle, for instance using a variable optical delay line. Since $|\alpha|^2 \ll 1$ in order to suppress multiphoton events ($n \geq 2$), the weak coherent pulses are primarily in the vacuum state. Quantum information protocols based on time-bin qubits are typically performed using prepare-and-measure schemes conditioned on single-photon detection, where quantum states are post-selected by single-photon detectors that measure the time-of-arrival states of the qubits.

Single photons can also be heralded from a pair source, where a signal photon is "heralded" by the detection of an idler photon (see Sec. 2.4). The output state of a photon pair produced by SPDC in a single temporal mode is described by the

two-mode squeezed vacuum state (TMSV),

$$|\text{TMSV}\rangle = \sum_{n=0}^{\infty}(-1)^n\sqrt{\frac{\mu^n}{(1+\mu)^{n+1}}}\,|n\rangle_s\,|n\rangle_i \tag{2.10}$$

$$\approx |0\rangle_i\,|0\rangle_s + \sqrt{\mu}\,|1\rangle_i\,|1\rangle_s + O(\mu) \quad \mu \ll 1. \tag{2.11}$$

Time-bin entangled states can be generated by pumping a photon pair source with a pair of strong pulses in early and late time bins (see Fig. 2.3b). The output state is described by the product state of a two-mode squeezed vacuum state (TMSV) in the early and late temporal modes,

$$|\text{TMSV}\rangle_e \otimes |\text{TMSV}\rangle_l \approx \sqrt{1-2\mu}\,|0\rangle + \sqrt{2\mu}\,\left|\Phi^+\right\rangle + O(\mu), \quad \mu \ll 1, \tag{2.12}$$

where $|0\rangle$ is the vacuum state, μ is the mean photon number, and

$$\left|\Phi^+\right\rangle = \frac{1}{\sqrt{2}}(|e\rangle_s\,|e\rangle_i + |l\rangle_s\,|l\rangle_i)$$

is a Bell state of signal (s) and idler (i) photons in the time-bin qubit basis. In Eq. 2.12, higher order terms of $O(\mu)$ correspond to multiphoton states, where $\mu \ll 1$ suppresses the probability of multiphoton events (see Sec. 2.4). A Bell state can be post-selected by conditioning on the coincident detection of signal and idler photons in either the early or late time-bin at spatially separated single-photon detectors. With photon pairs generated by type-II SPDC, for instance, Bell states can be conveniently distributed to different nodes in a network using a polarizing beamsplitter to separate signal and idler photons in orthogonal polarization states.

Continuous variables

For continuous variable protocols, quantum information is encoded in continuous DOFs, such as the amplitude and phase of the electromagnetic field quadratures, $\hat{Q}$ and $\hat{P}$. The Hamiltonian density ($\mathcal{H}$) of an electromagnetic field can be expressed in terms of the $\hat{Q}$ and $\hat{P}$ quadratures as,

$$\mathcal{H} = \frac{1}{2}(\hat{P}^2 + \omega^2\hat{Q}), \qquad \hat{P} = \frac{i(\hat{a} - \hat{a}^\dagger)}{\sqrt{2}}, \quad \hat{Q} = \frac{(\hat{a} + \hat{a}^\dagger)}{\sqrt{2}} \tag{2.13}$$

where $\hat{a}$ and $\hat{a}^\dagger$ are the pair of bosonic annhiliation and creation operators satisfying $[\hat{a}^\dagger, \hat{a}] = 1$, such that $[\hat{Q}, \hat{P}] = i$. Quantum states can be described as a function of the quadrature observables Q and P in phase space by the Wigner quasiprobability distribution, $W(Q, P)$. Gaussian states of light, characterized by Gaussian Wigner distributions, are commonly used as carriers of CV information due to their ease of

generation. The Wigner distributions of Gaussian states such as vacuum, coherent, and squeezed states are illustrated in Fig. 2.4, where the widths of the distributions are constrained by the Heisenberg uncertainty principle, $\Delta Q \Delta P \geq 1/4$. Vacuum and coherent states are represented by symmetric Gaussian distributions in phase space that saturate the uncertainty principle with $\Delta Q^2 = \Delta P^2 = 1/2$. Squeezed states are represented by ellipical Gaussian distributions in phase space characterized by a "squeezed" quadrature (Q) and "antisqueezed" quadrature (P), where the squeezed quadrature exhibits an uncertainty below ($\Delta Q^2 < 1/2$) and the antisqueezed quadrature exhibits an uncertainty above ($\Delta P^2 > 1/2$) the vacuum quadrature uncertainty.

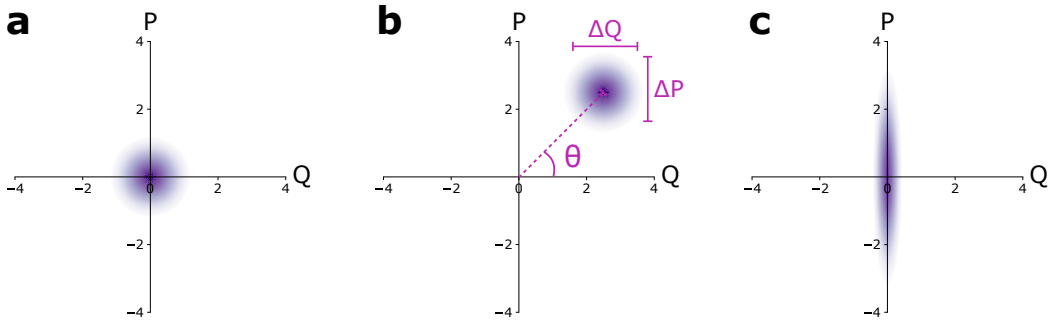

Figure 2.4: Wigner quasiprobability distribution $W(Q, P)$ for a) the vacuum state, b) a coherent state with $\alpha = 2.5$ and $\theta = \pi/4$, c) a squeezed vacuum state with $r = 1$, where Q is the squeezed quadrature and P is the antisqueezed quadrature.

Squeezing Squeezed states form an essential resource for many CV quantum protocols, including sub-shot noise sensing, CV quantum teleportation, and measurement-based quantum computing. Mathematically, squeezed states can be described by the action of the squeezing operator, $\hat{S}_1(r)$, on the vacuum state, [28],

$$\hat{S}_1(r)\,|0\rangle = \exp\left(\frac{r\hat{a}^2 - r^*\hat{a}^{\dagger 2}}{2}\right)|0\rangle\,, \tag{2.14}$$

where the squeezing parameter r determines the amount of squeezing and $\hat{a}$ and $\hat{a}^\dagger$ are the bosonic ladder operators satisfying $[\hat{a}^\dagger, \hat{a}] = 1$. The action of the squeezing operator can be modeled as the evolution of the vacuum state under the Hamiltonian,

$$\hat{H}_1 = i\hbar\alpha(r\hat{a}^2 - r^*\hat{a}^{\dagger 2})/2, \tag{2.15}$$

with time $t = r/\alpha$ such that $\hat{S}_1(r) = \exp\left(-i\hat{H}_1 t/\hbar\right)$. In the Heisenberg picture, the ladder operators evolve as,

$$\frac{d\hat{a}}{dt} = \frac{i}{\hbar}[\hat{H}_1, \hat{a}] = -\alpha\hat{a}^\dagger \tag{2.16}$$

$$\frac{d\hat{a}^\dagger}{dt} = \frac{i}{\hbar}[\hat{H}_1, \hat{a}^\dagger] = -\alpha\hat{a}. \tag{2.17}$$

After evolution over a time $t = r/\alpha$, the ladder operators are transformed as,

$$\hat{a}(r) = \hat{a}(0)\cosh r - \hat{a}^\dagger(0)\sinh r, \tag{2.18}$$

$$\hat{a}^\dagger(r) = \hat{a}^\dagger(0)\cosh r - \hat{a}(0)\sinh r, \tag{2.19}$$

referred to as a Bogoliubov transformation. The quadrature operators are transformed as,

$$\hat{Q}(r) = \frac{1}{\sqrt{2}}(\hat{a}(r) + \hat{a}^\dagger(r)) = \hat{Q}(0)e^{-r}, \tag{2.20}$$

$$\hat{P}(r) = \frac{1}{i\sqrt{2}}(\hat{a}(r) - \hat{a}^\dagger(r)) = \hat{P}(0)e^{r}, \tag{2.21}$$

which corresponds to squeezing of $\hat{Q}$ by a factor of e^{-r} and antisqueezing of $\hat{P}$ by a factor of e^r.

The state generated by $\hat{S}_1$ in Eq. 2.14 is a single mode squeezed vacuum (SMSV) state,

$$|\text{SMSV}\rangle = \hat{S}_1(r)\,|0\rangle = \sum_{n=0}^{\infty}(-1)^n\sqrt{\frac{\mu^n}{(1+\mu)^{n+1}}}\,|2n\rangle \tag{2.22}$$

$$\approx |0\rangle - \sqrt{\mu}\,|2\rangle + O(\mu), \qquad \mu \ll 1 \tag{2.23}$$

where $\mu = \langle\hat{a}^\dagger(r)\hat{a}(r)\rangle = \sinh^2(r)$ is the mean photon number. The two-mode squeezed vacuum state (TMSV) is generated by the action of the squeezing operator $\hat{S}_2(r)$ on the vacuum state,

$$|\text{TMSV}\rangle = \hat{S}_2(r)\,|0\rangle = \exp\left(\frac{r\hat{a}_1\hat{a}_2 - r^*\hat{a}_1^\dagger\hat{a}_2^\dagger}{2}\right)|0\rangle\,, \tag{2.24}$$

$$= \sum_{n=0}^{\infty}(-1)^n\sqrt{\frac{\mu^n}{(1+\mu)^{n+1}}}\,|n\rangle\,|n\rangle\,, \tag{2.25}$$

$$\approx |0\rangle\,|0\rangle - \sqrt{\mu}\,|1\rangle\,|1\rangle + O(\mu), \qquad \mu \ll 1, \tag{2.26}$$

which is expanded in the Fock basis in Eq. 2.25. The squeezing operator $\hat{S}_2(r)$ has the associated Hamiltonian $\hat{H}_2 = i\hbar\alpha(r\hat{a}_1\hat{a}_2 - r^*\hat{a}_1^\dagger\hat{a}_2^\dagger)/2$, which corresponds to the SPDC interaction Hamiltonian in Eq. 2.3.

Squeezed states of light can be prepared experimentally by nonlinear optical processes such as SPDC and SFWM. SMSV states can be produced by degenerate SPDC with collinear phase matching, for instance using a type-0 SPDC source, and TMSV states can be produced by non-degenerate SPDC, for instance using a type-I or type-II SPDC source. The experimental generation of single-mode squeezed light at telecom wavelength using commerically-available, fiber-coupled components is illustrated in Fig. 2.5a. To extract information encoded in the quadratures, quadrature measurements are typically performed using balanced homodyne detection (BHD) [29, 30]. In homodyne detection, a weak signal field ($\hat{a}$) is interfered with a strong local oscillator ($\hat{b}$) at a 50:50 beamsplitter, and the light from each output,

$$\hat{c} = \frac{1}{\sqrt{2}}(\hat{a} + \hat{b}), \tag{2.27}$$

$$\hat{d} = \frac{1}{\sqrt{2}}(\hat{a} - \hat{b}), \tag{2.28}$$

is detected by a photodiode (PD). The current from each photodiode is proportional to the mean photon number of the incident light,

$$\langle \hat{i}_c \rangle \propto \langle \hat{c}^\dagger \hat{c} \rangle = \frac{\langle \hat{a}^\dagger \hat{a} \rangle + \langle \hat{a}^\dagger \hat{b} \rangle + \langle \hat{b}^\dagger \hat{a} \rangle + \langle \hat{b}^\dagger \hat{b} \rangle}{2}, \tag{2.29}$$

$$\langle \hat{i}_d \rangle \propto \langle \hat{d}^\dagger \hat{d} \rangle = \frac{\langle \hat{a}^\dagger \hat{a} \rangle - \langle \hat{a}^\dagger \hat{b} \rangle - \langle \hat{b}^\dagger \hat{a} \rangle + \langle \hat{b}^\dagger \hat{b} \rangle}{2}. \tag{2.30}$$

The photodiodes are in a balanced configuration where the photocurrents are subtracted, resulting in an output current proportional to the quadrature of the signal field,

$$\langle \hat{i}_c - \hat{i}_d \rangle \propto \frac{\langle \hat{b}^\dagger \hat{a} \rangle + \langle \hat{a}^\dagger \hat{b} \rangle}{\sqrt{2}} \approx |\beta| \langle \hat{Q}(\theta) \rangle, \tag{2.31}$$

where $\hat{Q}(\theta) = (\hat{a}e^{-i\theta} + \hat{a}^\dagger e^{i\theta})/\sqrt{2}$. The approximation is taken in the limit of a strong local oscillator in a coherent state $|\beta\rangle$, using the substitution $\hat{b} \rightarrow |\beta| e^{i\theta}$ where θ is the relative phase of the signal and local oscillator. States of the signal field can be probed in phase space by sweeping the phase of the local oscillator, where setting $\theta = 0$ and $\theta = \pi/2$ corresponds to projections onto $\hat{Q}$ and $\hat{P}$, respectively. The state of the signal field can reconstructed by measuring the BHD output with a signal analyzer and acquiring quadrature statistics over various phases from $\theta = [0, 2\pi]$ to form a tomographically complete set of measurements. An simulation of quadrature statistics for a squeezed vacuum state measured using an oscilloscope over various

phases is shown in Fig. 2.5b. The amount of squeezing can be characterized by comparing the measured quadrature variance of the squeezed state to that of the vacuum state. For a squeezed vacuum state, the quadrature mean is $\langle \hat{Q}_\theta \rangle = 0$, and the quadrature variance is,

$$\langle \Delta \hat{Q}_\theta^2 \rangle = \frac{1}{2}(e^{-2r}\cos^2\theta + e^{2r}\sin^2\theta). \tag{2.32}$$

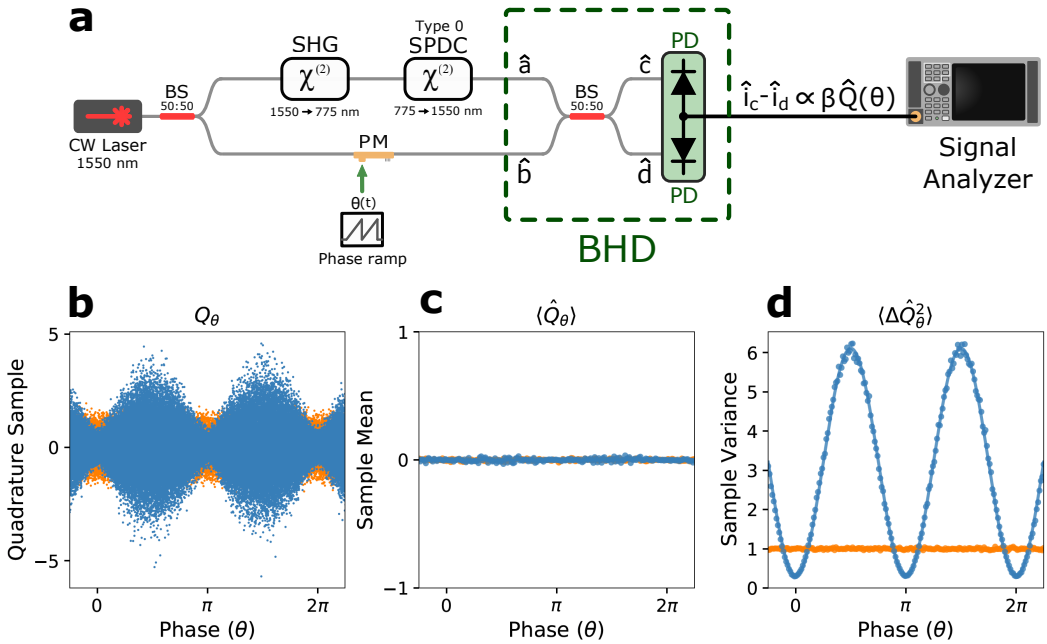

Figure 2.5: Generation of single-mode squeezed vacuum light at telecom wavelength with fiber-coupled components. a) Experimental setup. b)-d) Numerical simulation of quadrature statistics obtained from time-domain analyzer for a linear phase ramp applied to the LO. b) Quadrature samples as a function of time (phase) for a vacuum state (orange) and a squeezed vacuum state with a squeezing parameter of $r = 1$ and measurement efficiency of $\eta = 0.8$ (blue). c) Sample means and d) normalized sample variances as a function of time. The sample variances are normalized to the mean of the vacuum sample variances. The solid lines in c) and d) are the corresponding analytic predictions for the quadrature means and variances.

2.3 Detectors

Single-photon detectors

Quantum networks rely on high-fidelity single-photon detectors for state preparation and measurement. An optimal single-photon detector for quantum networking

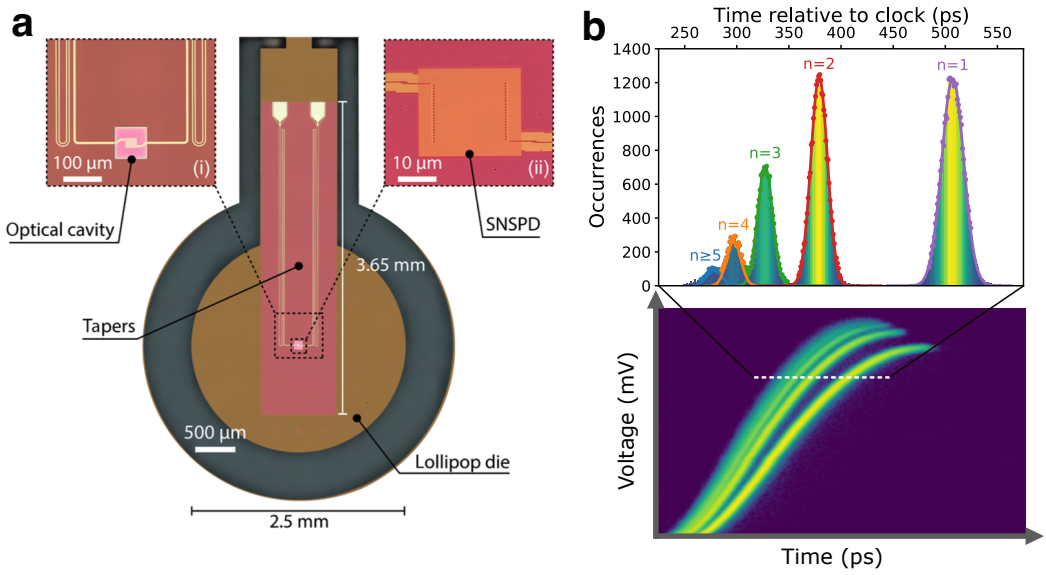

Figure 2.6: Photon-number-resolving superconducting nanowire detector. a) Optical micrograph of differential single-pixel superconducting nanowire single-photon detector.[a] b) Bottom: Measurement of RF readout pulses from impedance-matched tapered nanowire with oscilloscope in persistent mode. Photon number is encoded in the amplitude and slew rate of RF pulses. RF pulses are readout to a time-tagger with a constant voltage discriminator, where the variation in slew rate results in a variation of the registered time-tag. Top: Distribution of time-tags relative to a clock signal. Higher photon numbers correspond to higher slew rates and lower time-delays relative to the clock. Distinct Gaussian distributions of time-tags corresponding to photon number events are resolved up to 5 photons.

[a]Reprinted figure with permission from M. Colangelo, B. Korzh, J.P. Allmaras, A.D. Beyer, A.S. Mueller, R.M. Briggs, B. Bumble, M. Runyan, M.J. Stevens, A.N. McCaughan, and D. Zhu, "Impedance-matched differential superconducting nanowire detectors." Physical Review Applied, 19(4), p.044093. 2023. DOI: `https://doi.org/10.1103/PhysRevApplied.19.044093`. Copyright 2025 by the American Physical Society.

would couple unity efficiency with gigahertz-rate operation, picosecond timing jitter, negligible dark counts, and the ability to discriminate large photon numbers with high fidelity at telecom wavelengths [31, 32]. Transition-edge sensors [33, 34, 35, 36, 37] and MKIDs [38, 39] offer inherent photon-number-resolving (PNR) capability with high efficiency and low dark count rates, but their kilohertz-scale speeds and sub-Kelvin cooling conflict with the multi-gigahertz clock rates and field-deployable cryocoolers envisioned for regional links. Superconducting nanowire single-photon detectors (SNSPDs) are the leading detectors at telecom wavelengths, with up to 98% system efficiency [40], ultra low dark counts in the milli- to micro-hertz range [41], count rates $>$ 100 MHz per nanowire [42], sub-3ps timing jitter [43], and nanosecond reset times [44] demonstrated in the literature (see Fig. 2.6). In an SNSPD, a photon absorbed by a superconducting nanowire generates a time-dependent resistive hotspot, which results in a readout pulse at RF. SNSPDs are routinely used for quantum communication and already meet the speed, jitter, and operating-temperature targets for quantum networking; substantial efforts are underway to add PNR functionality to SNSPDs to complete the optimal detector performance set.

Recent progress in PNR SNSPDs follows two complementary paths. Microwave-engineered single pixel detectors use on-chip impedance-matching tapers to enhance the detector's signal-to-noise ratio so that the RF output pulse varies with photon number [45], allowing for the discrimination of up to five photons with an individual nanowire [46] while preserving picosecond-level timing and high count rates (see Fig. 15). Photon number can be extracted from the output pulse amplitude [47, 45, 48] or slew-rate [49] variation. The latter approach requires only a constant threshold voltage discriminator [27], which suitable for real-time readout with commercial time-taggers for scalable networking. A differential readout architecture optimizes the design of impedance-matched devices by canceling geometric delay-line contributions to the jitter, enabling low-jitter and large active area single pixel detectors with PNR capabilities [47]. Alternatively, quasi- photon number resolution can be achieved by spatial [50, 51, 52] or temporal [53, 54] multiplexing of detectors without requiring intrinsic PNR per pixel. To resolve photon number with high fidelity, the number of spatial or temporal bins needs to be significantly larger than the number of input photons, typically at the expense of increased complexity and low detection rate. Scalable waveguide-integrated arrays of nanowires connected in parallel [55, 56, 57] or series [58] extend the photon-count ceiling without sacrificing speed, enabling photon counting with high dynamic range. Re-

cent demonstrations include 1.5 GHz aggregate rates for a 14-pixel distributed array at 90% system efficiency [42] and a monolithic 100-pixel detector array that resolves 0–100 photons per pulse with sub-nanosecond reset time [59].

Balanced homodyne detectors

In addition to single-photon detectors, low noise and high bandwidth BHDs are needed to measure quadrature information in CV protocols, such as Gaussian-modulated CV quantum key distribution (QKD) [60], measurement-based quantum computing [61, 62], sub-shot noise quantum sensing [63]. Together, PNRD and BHDs form a complete detector set for universal fault-tolerant quantum computing [64, 65] as well as hybrid DV and CV protocols such as deterministic quantum teleportation [66].

The ideal BHD combines near-unity quantum efficiency, low optical loss, low electronic noise, > 1 GHz bandwidth, high common-mode rejection, and stable phase locking for real-time operation at telecom wavelengths.Although high quantum efficiencies ~ 99% [67] have been demonstrated with traditional BHDs using discrete photodiodes and bulk optics, they face challenges in scalability and phase-stability, particularly for large-scale systems [68] and field-deployable quantum networks. Recent progress in integrated quantum-limited BHDs addresses these limitations by leveraging integrated photonic platforms [69, 70], such as silicon photonics [71] and lithium niobate on insulator (LNOI) [72], for monolithic integration of the beamsplitter, phase shifter, and photodiodes on a chip (see Fig. 2.7). By integrating all on components on chip in a compact-form factor, photonic integrated circuits (PICs) can achieve high phase stability and scalability with high bandwidth electronic readout. In particular, silicon photonics enables large scale integration at telecom wavelengths [73, 74], with systems demonstrated with several thousands of components on chip [75], as well as interfacing with silicon electronics, such as low-noise transimpedance amplifiers (TIAs) and electronic integrated circuits (EICs), for readout and post-processing [76].

The use of integrated BHDs is increasingly motivated by the demands of large-scale quantum networks, where long-distance coherent communication over deployed telecom infrastructure requires detectors with low noise, high stability, and high bandwidths to enable high-speed quadrature measurements and phase tracking in the presence of channel dispersion and loss [79]. On-chip BHDs with co-integrated transimpedance amplifiers enable the highest achievable bandwidths by minimizing

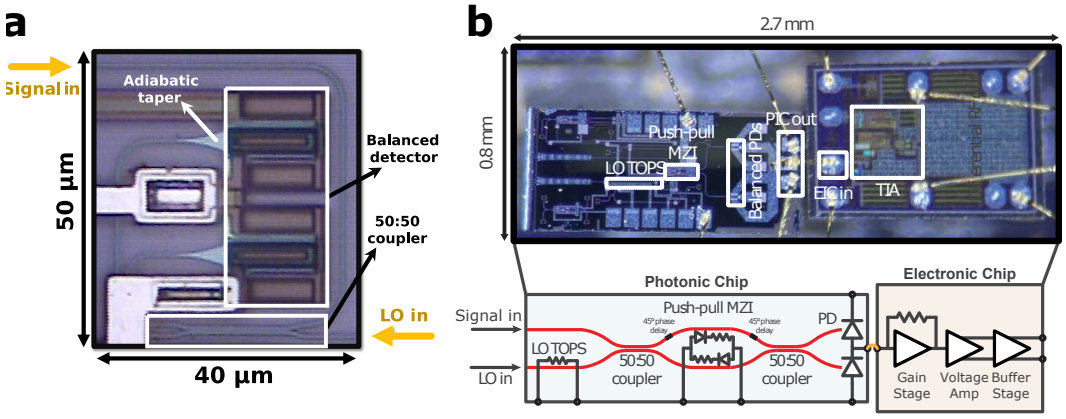

Figure 2.7: On-chip balanced homodyne detectors. a) Packaged die photo of an on-chip balanced homodyne detector from Gurses et al. (2023) [77]. b) Packaged die photo of photonic-electronic system for balanced homodyne detection from Gurses et al. (2024) [78]. The photonic chip contains a quantum-limited coherent receiver and wirebonded to the electronic chip with a transimpedance amplifier for readout.

parasitic capacitance and inductance, reducing interconnect lengths, and allowing co-design of the photodiode and amplifier circuitry. In contrast to bulk or discrete-component BHDs, where bandwidth is typically limited to the kHz-MHz range [80] due to long wirebonds, PCB traces, and large photodiode capacitance, integrated implementations eliminate these bottlenecks, preserve the amplifier's gain-bandwidth product, and enable multi-GHz operation [81]. Integration also allows precise impedance control, reduces signal degradation, and improves thermal and mechanical stability, making it essential for high-speed quantum optics applications requiring GHz-scale shot-noise-limited detection. For example, in CV-QKD and quantum random number generation (QRNG), high bandwidths directly translate to increased secure key rates and entropy generation, respectively. In quantum networks, integrated BHDs will be essential to meet the rate and distance requirements for metropolitan and backbone-level quantum repeaters, trusted-node links, and distributed quantum sensing architectures.

2.4 Heralded single-photon sources

Heralding of single photons is a common approach to produce spectrally tunable and indistinguishable photons with high purity and bandwidths. A bulk optical nonlinearity is used to probabilistically emit photon pairs via a $\chi^{(2)}$ or $\chi^{(3)}$ process, where an individual photon (in a signal mode) is "heralded" by the detection of the other photon (in an idler mode). Typically, a threshold detector is used to

discriminate between the presence of vacuum and at least one photon in the idler mode, which heralds the presence of photons in the signal mode. Heralding rates of $\sim 10^4 - 10^5$ pairs/s [82], system efficiencies of $20 - 30\%$ [82, 83], and $g^2(0) \sim 0.02 - 0.05$ [84, 18] have been demonstrated using bulk single pass SPDC sources and avalanche photodiode detectors. Spatial and spectral mode engineering can be employed to optimize the efficiency and purity, with demonstrations of up to 60% system efficiency using waveguides [84] and cavity-enhanced collection efficiency [85] as well as > 0.90 spectral factorability via pulse engineering [84] and narrowband filtering [85]. However, the emission of multiphoton pairs that contaminate the heralding restrict single-photon generation to low probability (e.g., $\mu \sim 10^{-3}$ in practice). The probability of n emitted photon pairs follows the thermal distribution, $P(n) = \mu^n/(1+\mu)^{n+1}$. Therefore, there is a trade-off in the single-photon heralding rate $\sim \mu$ and single-photon fidelity due non-negligible multiphoton pair production probability $P(n > 1)$ for increased μ [86].

Improving HSPS with PNR SNSPD

To overcome this challenge, a photon-number-resolving (PNR) detector can be used to filter out multiphoton pair events by discriminating the presence of vacuum, one photon, or multiple photons. By excluding multiphoton events at the idler mode, PNR detectors enable the heralding of single photons with high fidelities. Due to their combination of high detection efficiency, low dark counts, fast recovery time, and low jitter, PNR SNSPDs are desirable for heralding single photons at high rates. In Chapter 3, I report the first demonstration of heralding single photons with a PNR SNSPD. Using an efficient and low noise photon-number-resolving superconducting nanowire detector we herald, in real time, a single photon at telecommunication wavelength. We perform a second-order photon correlation $g^2(0)$ measurement of the signal mode conditioned on the measured photon number of the idler mode for various pump powers and demonstrate an improvement of a heralded single-photon source. We develop an analytical model using a phase-space formalism that encompasses all multiphoton effects and relevant imperfections, such as loss and multiple Schmidt modes. We perform a maximum-likelihood fit to test the agreement of the model to the data and extract the best-fit mean photon number μ of the pair source for each pump power. A maximum reduction of 0.118 ± 0.012 in the photon $g^2(0)$ correlation function at $\mu = 0.327 \pm 0.007$ is obtained, indicating a strong suppression of multiphoton emissions. For a fixed $g^2(0) = 7 \times 10^{-3}$, we increase the single pair generation probability by 25%. Our experiment, built using

fiber-coupled and off-the-shelf components, delineates a path to engineering ideal sources of single photons.

2.5 Entanglement distribution

High-fidelity entanglement distribution is an essential functionality of quantum networks. Entanglement is a key resource for a range of quantum communication protocols, including entanglement-based QKD, Bell tests and quantum teleportation. By splitting photon pairs produced by SPDC, entangled photons can be distributed to distant nodes over long distances in optical fiber or free space. However, experimental imperfections such as multiphoton noise and loss degrade the state fidelity of entangled photons over long distances. To evaluate the fidelity of distributed entanglement, the entanglement visibility is a commonly used metric. The experimental setup for the characterization of entanglement visibility with time-bin entangled photon pairs is illustrated in Fig. 2.8. Interferometers are used perform projective measurements on time-qubits. By measuring counts in the first and third bins at the output of interferometer, project on computational (Pauli Z) basis states E and L, respectively. By measuring counts in the middle bins, project onto phase basis state of the form $(|e\rangle + e^{i\varphi}|l\rangle)/\sqrt{2}$, where φ is set tuning the the interferometric phase. Projections onto the Pauli X basis states $(|e\rangle \pm |l\rangle)/\sqrt{2}$ and Pauli Y basis states $(|e\rangle \pm i|l\rangle)/\sqrt{2}$ by setting $\varphi = \pm\pi/2$ and $\varphi = 0, \pi$, respectively.

At Alice and Bob, counts measured in individual bins correspond to projections onto the mixed state

$$\rho^{A(B)} = \mathrm{Tr}_{B(A)}[\rho], \tag{2.33}$$

which is obtained by tracing out Bob's (B) and Alice's (A) subsystem, respectively, from the overall state $\rho \approx |\Phi^+\rangle\langle\Phi^+|$. This yields

$$\rho^{A(B)} = \frac{1}{2}(|e\rangle\langle e| + |l\rangle\langle l|) = \frac{1}{2}\mathbb{I}_2. \tag{2.34}$$

Therefore, counts measured in individual bins at Alice and Bob do not vary with φ, reflecting that each qubit individually carries no information—only their joint correlations are pure and maximally entangled. The phase-dependent quantum correlations are exhibited in the coincidence counts between the middle bins at Alice and Bob[1],

$$C_{AB}(\varphi) \propto \mathrm{Tr}[\rho\,|\varphi\rangle\langle\varphi|_A \otimes |\varphi\rangle\langle\varphi|_B] = \frac{1}{2}\cos^2\varphi, \tag{2.35}$$

[1]The coincidence counts between the first and third bins at Alice and Bob are constant (since $\mathrm{Tr}[\rho\,|e\rangle\langle e|_A \otimes |e\rangle\langle e|_B] = 1/2$ and $\mathrm{Tr}[\rho\,|l\rangle\langle l|_A \otimes |l\rangle\langle l|_B] = 1/2$).

where $|\varphi\rangle = (|e\rangle + e^{i\varphi}|l\rangle)/\sqrt{2}$. The entanglement visibility is defined as

$$V_{\text{ent}} = \frac{C_{AB}^{\max} - C_{AB}^{\min}}{C_{AB}^{\max} + C_{AB}^{\min}}. \tag{2.36}$$

The entanglement visibility V_{ent} quantifies the contrast of phase-dependent quantum correlations and ranges from 0 (no coherence) to 1 (perfect entanglement). Assuming the shared bipartite state can be modeled as a Werner state [87], the entanglement visibility directly relates to the fidelity with respect to the target Bell state as $F = \frac{1}{4}(1 + 3V_{\text{ent}})$. In this model, separable states satisfy the classical bound $V_{\text{ent}} \leq 1/3$, while any visibility above this threshold certifies the presence of quantum entanglement. However, not all entangled states exhibit nonlocal correlations strong enough to violate a Bell inequality. Bell non-locality is only observed when $V_{\text{ent}} > 1/\sqrt{2}$, which corresponds to violation of the CHSH inequality [88]. For applications in device-independent quantum key distribution (DI-QKD), even higher visibility is required to ensure robustness against noise and detector inefficiencies, with typical experimental thresholds around $V_{\text{ent}} \gtrsim 0.78$ [89]. These visibility bounds thus provide operational criteria for certifying entanglement and nonclassical correlations directly from interference fringe measurements.

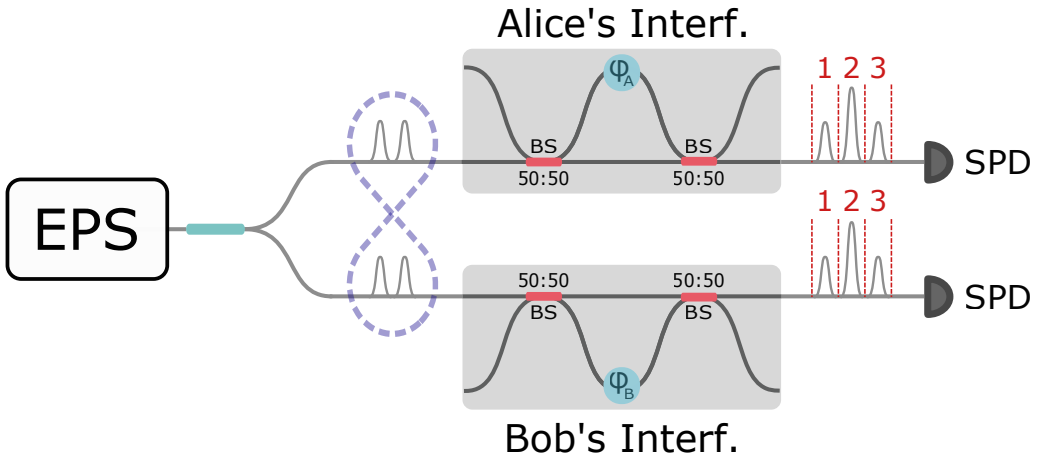

Figure 2.8: Experimental setup for measuring the entanglement visibility of time-bin qubits.

High-rate multiplexed entanglement source

Quantum networks require high-rate sources of entanglement that can maintain high entanglement visibilities over long distances. High entanglement generation rates are essential for overcoming photon losses in long-distance fiber or free-space links,

maintaining synchronization across the network, and providing high throughput for quantum communication protocols. In Chapter 5, I report a high-rate multiplexed entanglement source based on time-bin qubits for advanced quantum networks. We demonstrate a 4.09 GHz repetition rate source of photon pairs entangled across early and late time bins separated by 80 ps. Simultaneous high rates and high visibilities are achieved through frequency multiplexing the spontaneous parametric down-conversion output into 8 time-bin entangled channel pairs. We demonstrate entanglement visibilities as high as 99.4%, total entanglement rates up to 3.55×10^6 coincidences/s, and predict a straightforward path towards achieving up to an order of magnitude improvement in rates without compromising visibility. Finally, we resolve the density matrices of the entangled states for each multiplexed channel and express distillable entanglement rates in ebit/s, thereby quantifying the tradeoff between visibility and coincidence rates that contributes to useful entanglement distribution. This source is a fundamental building block for high-rate entanglement-based QKD systems or advanced quantum networks.

2.6 On-chip squeezed light detection

On-chip BHDs have been demonstrated with shot noise clearance exceeding 14 dB, bandwidths above 2.5 GHz, and total detection losses below 3.5 dB for Gaussian-modulated CV-QKD [90, 91, 92, 93] and quantum random number generation [94, 95, 96]. However, most demonstrations have been limited to the measurement of coherent or vacuum states, which have less stringent performance criteria compared to genuinely non-classical states. In particular, the detection of squeezed states, which are central to sub-shot-noise-limited sensing and continuous-variable cluster state generation for measurement-based quantum computing, is highly sensitive to both optical loss and effective loss from electronic noise [97, 98]. Moreover, there is a trade-off between shot noise clearance and bandwidth: increasing the transimpedance gain improves SNC by reducing input-referred noise, but narrows the bandwidth due to larger RC time constants. Conversely, widening the bandwidth by lowering gain increases electronic noise, thereby degrading sensitivity to quantum correlations.

To address these challenge, we develop integrated BHDs for the detection of non-classical light. First, we measure squeezed light with the on-chip BHD depicted in Fig. 2.7a and an off-chip TIA to measure squeezed light and demonstrate phase locking of squeezing on-chip [77]. Then, we design a photonic-electronic integrated circuit, which we refer to as a quantum-limited coherent receiver (QRX), for on-

chip detection of squeezed light with an on-chip TIA for readout [78]. The QRX is depicted in Fig. 2.7b. The QRX is optimized across various performance metrics: detection loss, common-mode rejection ratio (CMRR), shot-noise clearance (SNC), and bandwidth [77, 78].The CMRR quantifies the ability of the detector to suppress common-mode classical noise, particularly from the local oscillator, due to imbalance in the directional coupler of photodiode configuration. The SNC quantifies the ratio of quantum shot noise to electronic noise, where the LO knee power (P_{knee}) is the minimum LO power required for the shot noise to exceed the electronic noise floor. The detection bandwidth is quantified by the 3dB bandwidth (BW_{3dB}) and shot noise-limited bandwidth (BW_{shot}), which are the frequencies at which the optoelectronic gain drops by 3 dB from its low-frequency value and at which the quantum signal becomes equal to the electronic noise, respectively. The characterizations for the on-chip BHD (Gurses et al. (2023) and the QRX (Gurses et al. (2024)) are summarized in Table 2.1.

Reference	**Loss**	**CMRR**	**SNC**	P_{knee}	BW_{3dB}	BW_{shot}	**PIC/EIC**
Porto et al. (2018) [99]	—	—	17 dB	199 μW	7 MHz	—	Y*/N
Tasker et al. (2021) [100]	3.3 dB	61 dB	14 dB	200 μW	1.7 GHz	9 GHz	Y/Y
Gurses et al. (2023) [77]	5.4 dB	20.4 dB	26 dB	34.6 μW	3 MHz	24.3 MHz	Y/N
Gurses et al. (2024) [78]	2.7 dB	92.3 dB	14.5 dB	315 μW	2.57 GHz	3.50 GHz	Y/Y

Table 2.1: Comparison of quantum-limited BHDs on chip with demonstrated non-classical light detection. *Photodetectors not integrated.

On-chip squeezed light detection with phase-locking

With the integrated coherent receiver chip, we measured squeezed light and demonstrated an easy-to-deploy phase-locking approach to lock onto the squeezed quadrature with the setup shown in Fig. 2.9a. Squeezed vacuum states were generated with a periodically-poled lithium niobate (PPLN) waveguide and fiber-coupled to the chip. Noise floor oscillations in the output with 4 Hz LO phase modulation were measured with an electrical spectrum analyzer (ESA). A 100-second trace was recorded for both squeezed vacuum states (red) and vacuum states (black). A 1-second section of this data is shown in Fig. 2.9b. Over 100 seconds, noise floors 0.226 ± 0.096 dB below and 0.408 ± 0.146 dB above shot noise level (SNL) were observed.

Phase locking in quantum coherent receivers is necessary for maintaining sub-shot-noise-limited sensitivities with squeezed light and enabling phase-determinate

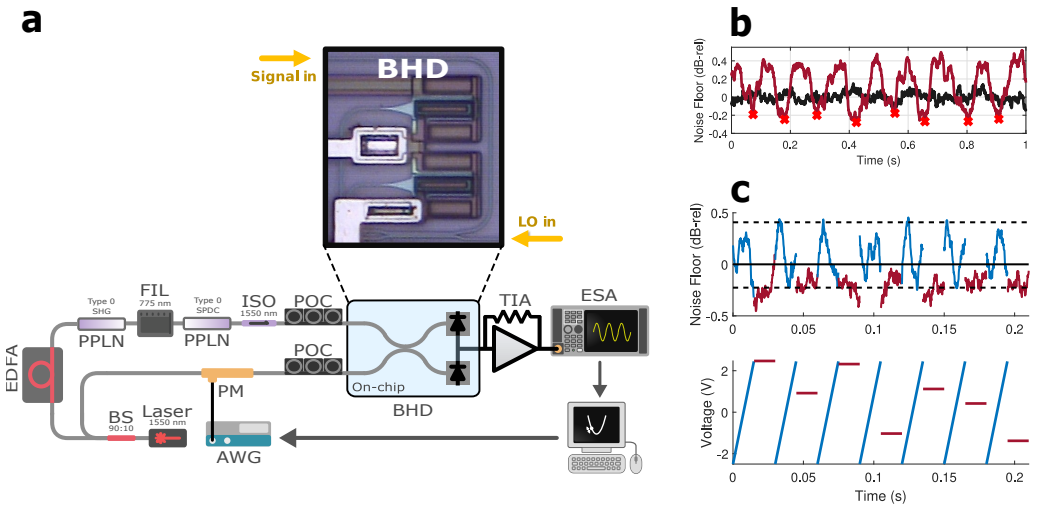

Figure 2.9: On-chip detection of squeezed light with optical phase locking. a) Setup with the silicon photonic receiver for squeezed light measurements. b) Oscillations between quadratures of the squeezed vacuum. Red crosses signify the squeezed quadrature. c) Demonstration of phase locking to the squeezed quadrature showing the noise floor (top) and modulator voltage (bottom)

quantum state tomography. A software-based phase-locking process can be useful for easily deploying coherent quantum links without the need for additional hardware in a quantum coherent transceiver system. Therefore, a phase-locking algorithm was employed to phase-lock the squeezed vacuum detected on-chip to its squeezed quadrature. The algorithm utilizes the phase modulator to do a π phase sweep and finds the phase voltage setting for the squeezed quadrature. The voltage setting is then applied to set the phase to the squeezed quadrature. This procedure is repeated at 67 Hz, as shown in Fig. 2.9c. This closed-loop phase locking approach enables sustained operation at sensitivities below the shot noise floor.

High bandwidth on-chip squeezed light detection

The QRX was used to measure squeezed vacuum to demonstrate sub-shot-noise level operation up to 3.5 GHz with integrated electronic TIA. The experimental setup is shown in Fig. 2.10b. Squeezed vacuum states were generated with a PPLN waveguide and fiber-coupled to the photonic chip with a V-groove array. Noise floor oscillations in the output with 1 Hz LO phase modulation were measured with a spectrum analyzer at different sideband frequencies up to the shot-noise-limited bandwidth Fig. 2.10c. Thirty-second traces were recorded for both squeezed vacuum states (red) and vacuum states (black) at each frequency. A ten-second

section of the data measured at 1.17 GHz is shown in Fig. 2.10d. After data collection, a peak search algorithm was used to acquire the noise level for squeezed and anti-squeezed quadratures normalized to the shot noise level (SNL) at each frequency. A maximum squeezed noise of 0.156 ± 0.039 dB below the SNL and a maximum anti-squeezed noise of 0.507 ± 0.052 above the SNL were observed, see Fig. 2.10e.

While we were limited by the source and tabletop component losses in the squeezed light measurements, on-chip loss sets the bound on how much squeezing can be observed with the QRX. The on-chip system loss comprises the optical losses and the optoelectronic loss determined by the shot noise clearance and PD quantum efficiency (QE). The QRX has a total optical loss of 2.7 dB with 1.3 dB from edge couplers, 1.4 dB from PD QE, and a negligible amount of loss from the TOPS, MZI, and routing. As shown in Fig. 2.10c, the shot noise clearance is also greater than 10 dB up to 2.24 GHz. Therefore, the system loss is at most 3 dB over the bandwidth of the receiver, enabling sensitivities of 3 dB below the SNL.

The packaged photonic-electronic QRX enables a path toward the deployment of quantum-limited coherent receivers in optical communication and sensing networks. Due to its compact size, high CMRR, highest reported 3-dB bandwidth and lowest reported system loss in the literature, it introduces the prospect of leveraging non-classical states of light to enhance the information capacity and sensitivity of optical links. With the demonstration of high shot-noise-limited bandwidth and detection of squeezed vacuum showcasing an enhancement in the SNL, this work highlights the potential of leveraging non-classical light and deploying quantum coherent receivers in classical optical networks in addition to preparing an infrastructure suitable for quantum communications.

Multiplexed BHD array on-chip for squeezed light detection

Beyond single component demonstrations, the next major milestone for CV quantum technologies is to develop large-scale quantum photonic systems on-chip, enabling massively parallelized operations with precise control in a compact form factor. While bulk optical experiments have demonstrated foundational protocols, they do not scale to the system sizes required for advanced and practical implementations of quantum technologies, such as computational quantum advantage or fault-tolerant error correction. Silicon photonics offers a CMOS-compatible platform that allows wafer-scale fabrication of stable, programmable optical circuits incorporating

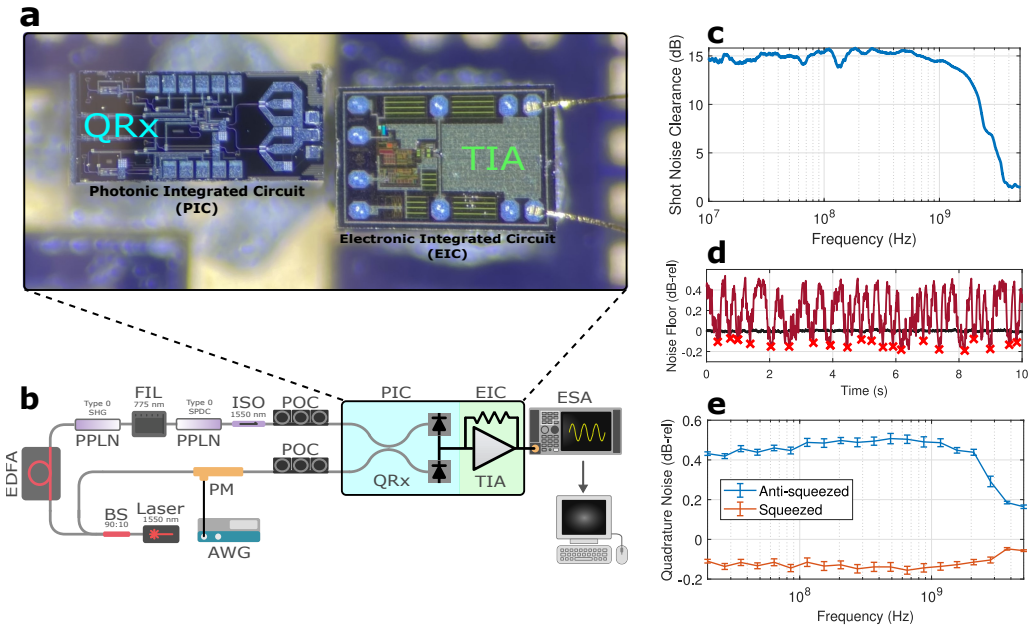

Figure 2.10: On-chip detection of squeezed light with a photonic-electronic integrated circuit. a) Die photo of photonic integrated circuit (PIC) for the quantum-limited coherent receiver (QRX) with high bandwidth photodiodes and electronic integrated circuit (EIC) for readout with a transimpedance amplifier (TIA). b) Setup with the integrated photonic-electronic coherent receiver for squeezed light measurements. c) Shot noise clearance response of the QRX with maximum LO photocurrent. d) Oscillations between quadratures of the squeezed vacuum measured at 1.17 GHz. Red crosses signify the squeezed quadrature. e) Quadrature noise normalized to the shot noise level of vacuum for squeezed and anti-squeezed quadratures.

sources, circuits, and detectors on a single chip. Advanced CV quantum technologies will require quadrature measurements across many spatial or temporal modes, critical for applications in distributed quantum sensing, measurement-based quantum computing, and broadband quantum communication. Multiplexed BHD array architectures have been proposed to boost rates in quantum random number generation (QRNG) and continuous-variable quantum key distribution (CV-QKD), enable entanglement-enhanced distributed quantum sensing, and perform mode-selective measurements in continuous-variable optical homodyne tomography. However, all demonstrations of multiplexed BHD systems to date have relied on bulk optics.

In Chapter 6, I report the first array of quantum-limited BHDs capable of detecting squeezed light on a silicon photonic chip. Scaling from a single QRX to a large-scale system introduces several design challenges, including minimizing electrical

parasitics to avoid RF oscillations, ensuring signal integrity across all channels, and suppressing electronic and optical crosstalk between densely packed channels. Using the QRX design in Fig. 2.7b as a blueprint, we spatially multiplex 32 QRXs on a silicon photonic chip. The outputs of the QRXs are wire-bonded to an interposer on a compact PCB containing an array of 32 discrete TIAs. We mitigate these challenges with a careful co-design between the photonic chip layout and electronic readout circuit. As described in the next section, the QRX array is incorporated into a larger system on the same chip, which is designed to demonstrate the basic functionalities required for chip-based wireless quantum technologies.

2.7 Quantum phased arrays

The expansion from wired to wireless links is an exciting prospect for integrated quantum technologies. For classical technologies, the advent of phased arrays enabled directional and adaptive wireless links by manipulating electromagnetic waves over free space. In a point-to-point wireless communication link, a transmitter encodes a signal in a beam of electromagnetic radiation that is sent to a receiver. The spot size of the beam spreads with distance due to diffraction, resulting in geometric loss from the overlap of the diverging spot size and the receiver aperture area. Diffraction-induced geometric loss can result in severe signal loss that ultimately limits the range and rate of communication [101, 102, 103, 104]. In classical wireless communications and sensing, beam divergence is controlled by wavefront engineering with transmitter or receiver phased arrays. A phased array is a coherent array of antenna elements that can transmit or receive electromagnetic fields. By controlling the amplitude and phase on each element, the wavefront of the electromagnetic field can be engineered over free space. Wavefront engineering allows for active manipulation of an electromagnetic field in a dynamic real-time fashion [105, 106]. Beamforming, or angular focusing, of an electromagnetic field is performed by coherently combining elements in a phased array such that the signal field constructively interferes at a selected angle [107].

Here I extend wavefront engineering to quantum fields with a concept referred to as "quantum phased arrays." A quantum phased array (QPA) is a quantum-coherent array of antenna elements, each with phase and amplitude control, that can emit or receive quantum fields. I show how beamforming with a QPA can be used to establish reconfigurable wireless quantum links for free-space quantum communications. More broadly, I demonstrate how to synthesize quantum states in the far-field with a QPA and illustrate how free-space protocols can be constructed

based on quantum state engineering with multiple QPAs.

Theory

A quantum field with annihilation operator $\hat{a}_{\text{in}}$ is input to a QPA transmitter. The field is distributed to N channels with associated spatial mode functions,

$$\hat{a}_{\text{in}} = \int \hat{a}_{\text{in}}(\rho) d\rho \tag{2.37}$$

$$\hat{a}_{\text{in}}(\rho), = \sum_{j=1}^{N} \hat{a}_j \mathcal{E}_j(\rho), \tag{2.38}$$

where $\hat{a}_j$ is the annhiliation operator for the jth channel mode. In each channel, a gain and phase shift is applied, followed by a radiation by an antenna. The antennas have an associated set of mode functions $\{\mathcal{E}_j(\rho)\}$, where $j = 1, ..., N$ and the aperture coordinates are grouped into ρ. The channel modes are related to the aperture spatial modes by,

$$\hat{a}_j = \int \mathcal{E}_j(\rho) \hat{a}_{\text{in}}(\rho) d\rho, \tag{2.39}$$

where $\hat{a}_{\text{in}}(\rho)$ is the creation operator for the field distributed to location ρ.

The field at the output of the aperture is,

$$\hat{a}_{\text{out}} = \int \hat{a}_{\text{out}}(\rho) d\rho, \tag{2.40}$$

$$\hat{a}_{\text{out}}(\rho) = \sum_{j} g_j e^{i\phi_j} \hat{a}_j \mathcal{E}_j(\rho), \tag{2.41}$$

where g_j is the gain and ϕ_j is the phase applied to each channel mode $\hat{a}_j$.

In the small pixel and large N limit, the pixel mode functions approach,

$$\mathcal{E}_j(\rho) \approx \delta^d(\rho - \rho_j), \tag{2.42}$$

where $\delta^d(\rho)$ is the d dimensional Delta function with d denoting the coordinate dimensions, ρ_j represents the coordinates of the center of the jth pixel. In this limit, $\hat{a}_j \approx \hat{a}_{\text{in}}(\rho_j)\Delta\rho_j$ where $\Delta\rho_j$ is the surface area of the jth pixel, and the output field becomes,

$$\hat{a}_{\text{out}}(\rho) = \sum_{j} g_j e^{i\phi_j} \hat{a}_{\text{in}}(\rho_j) \delta^d(\rho - \rho_j) \Delta\rho_j, \tag{2.43}$$

$$\approx \int g(\rho_j) e^{i\phi(\rho_j)} \hat{a}_{\text{in}}(\rho_j) \delta^d(\rho - \rho_j) d\rho_j, \tag{2.44}$$

$$= c(\rho) \hat{a}_{\text{in}}(\rho), \tag{2.45}$$

where the sum in Eq. 2.43 becomes a Riemann sum over the antenna coordinates and the applied gains $\{g_j\}$ and phases $\{\phi_j\}$ approach continuous gain $g(\rho_j)$ and phase $\phi(\rho_j)$ profiles, respectively. The gain and phase profiles give rise to a reconfigurable array mode function, $c(\rho) = g(\rho)e^{i\phi(\rho)}$, that can be used to engineer quantum states at the focal plane of the QPA.

In the far field limit, the field at the aperture plane can be approximated in terms of the field at focal plane by the Kirchhoff-Fresnel diffraction formula (see Methods in Chapter 6),

$$\hat{a}_{\text{out}} = \int c(\rho)\hat{a}_{\text{in}}(\rho)d\rho \approx \int c(f)\hat{a}_{\text{in}}(f)df, \tag{2.46}$$

where $f = \sin\theta/\lambda$ is the focal plane coordinate and the focal plane mode profile is,

$$c(f) \propto \int e^{i2\pi\rho f} c(\rho)d\rho. \tag{2.47}$$

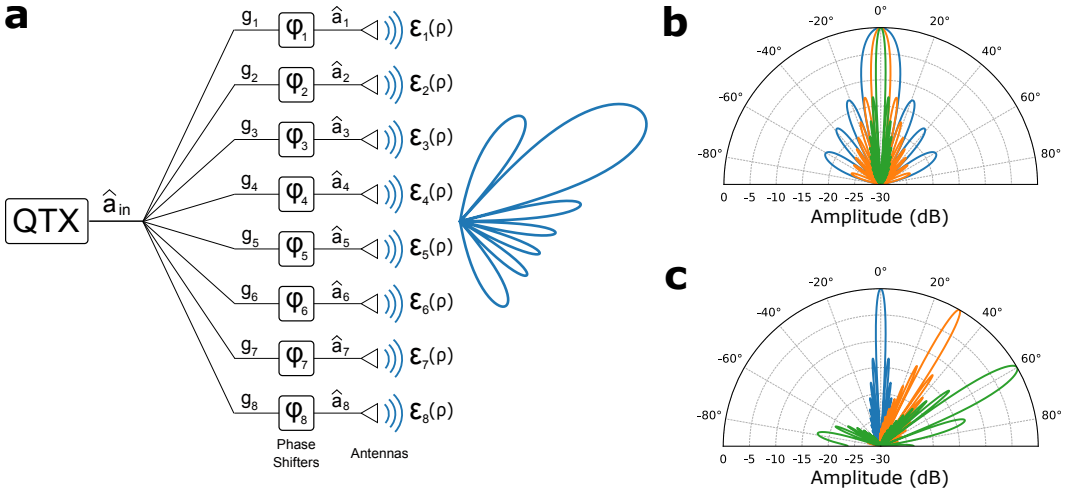

Figure 2.11: Quantum phased array transmitter. a) Conceptual diagram of a quantum phased array transmitter. The QTX is a source of a quantum states of an electromagnetic field $\hat{a}_{\text{in}}$, which is distributed across eight antenna elements. An amplitude g_n and phase shift φ_n is applied to each element, and the field from each antenna with a mode function $\mathcal{E}_n(\rho)$ is radiated to free-space, where $n \in [1, 8]$. b) Array factor for a uniform linear array of eight (blue), sixteen (orange), and 32 (green) elements, beamformed at broadside. c) Array factor for a uniform linear array of 32 elements beamformed at broadside (blue), 30° (orange), and 60° (green).

Array factor: Consider an N-element linear array with uniform amplitude and spacing,

$$\hat{a}_{\text{out}}(\rho) = \sum_{j=1}^{N} e^{i\phi_j} \hat{a}_j \mathcal{E}_j(\rho). \tag{2.48}$$

In the small pixel limit,

$$\hat{a}_{\text{out}} \approx \sum_{j} e^{i\phi_j} \hat{a}_{\text{in}}(\rho_j) \Delta\rho_j, \tag{2.49}$$

$$= \int \left(\sum_{j=1}^{N} e^{i\phi_j} \delta(\rho - \rho_j) \Delta\rho_j \right) \hat{a}_{\text{in}}(\rho) d\rho. \tag{2.50}$$

In terms of focal plane coordinates,

$$\hat{a}_{\text{out}} \propto \int \left(\sum_{j=1}^{N} e^{i(\phi_j + 2\pi\rho_j f)} \right) \hat{a}_{\text{in}}(f) df. \tag{2.51}$$

The coefficients in parentheses is the modal profile of beam in focal plane and corresponds to the array factor (AF) of the phased array [108],

$$\text{AF}(f, \beta) = \sum_{j=1}^{N} e^{i(\phi_j + 2\pi\rho_j f)}. \tag{2.52}$$

For an array with a progressive phase $\Delta\phi$ applied to the antennas that are uniformly spaced by a distance d, corresponding to $\phi_j = \Delta\phi(j-1)$ and $\rho_j = (j-1)d$, the array factor is [108],

$$\text{AF}(f, \beta) = e^{i[(N-1)/2]\varphi} \left[\frac{\sin\left(\frac{N}{2}\varphi\right)}{\sin\left(\frac{1}{2}\varphi\right)} \right], \tag{2.53}$$

where $\varphi = \Delta\phi + (2\pi d/\lambda)\sin\theta$. In normalized form, the array factor is,

$$\text{AF}_N(\varphi) = \frac{\sin\left(\frac{N}{2}\varphi\right)}{N \sin\left(\frac{1}{2}\varphi\right)} \approx \text{sinc}\left(\frac{N}{2}\varphi\right), \tag{2.54}$$

where the approximation is taken in small φ. The normalized array factor is plotted in Fig. 2.11b for $N = 8, 16$ and 32.

Beam steering: The maximum of AF_N occurs when $\varphi = 0$ at,

$$\theta_{\text{max}} = \arcsin\left(-\frac{\lambda\Delta\phi}{2\pi d}\right). \tag{2.55}$$

The beam maximum can be steered by varying the progressive phase $\Delta\phi$. The array factor for various beam angles θ_{max} are shown in Fig. 2.11c.

Beamwidth: The 3 dB point of the beam occurs for Eq. 2.54 when,

$$\theta_h^{\pm} = \arcsin\left[\frac{\lambda}{2\pi d}\left(-\Delta\phi \pm \frac{2.782}{N}\right)\right]. \tag{2.56}$$

The half-power beamwidth for a symmetrical pattern is $\Theta_h = 2|\theta_{\max} - \theta_h^-|$ [108]. For $d \gg \lambda$, $\Theta_h \sim \frac{\lambda}{Nd}$. The beamwidth scales inversely with the aperture width Nd. For large N, $\hat{a}_{\text{out}} \to \hat{a}_{\text{in}}(f_{\max})$ where $f_{\max} = \sin(\theta_{\max})/\lambda$.

Quantum state synthesis

For a target state in the focal plane, the coefficients for the aperture plane profile can be found in terms of the desired focal plane coefficients as,

$$c(\rho) \propto \int e^{-i2\pi\rho f} c(f) df. \tag{2.57}$$

Superposition states can be engineered by synthesizing multimode radiation patterns. For an N-element uniform linear array, a two-mode superposition state can be realized by,

$$\hat{a}_{\text{out}}(\rho) = \sum_{j=1}^{N} \frac{1}{\sqrt{2}}\left(e^{i\phi_j^A} + e^{i\delta}e^{i\phi_j^B}\right)\hat{a}_j \mathcal{E}_j(\rho), \tag{2.58}$$

where $\phi_j^A = \Delta\phi^A(j-1)$ and $\phi_j^B = \Delta\phi^B(j-1)$. The resulting array factor is the superpositon of the array factors,

$$\text{AF}_N = \frac{1}{\sqrt{2}}\left(\text{AF}_N(\varphi^A) + e^{i\delta}\text{AF}_N(\varphi^B)\right), \tag{2.59}$$

which in the large N limit approaches the superposition state,

$$\hat{a}_{\text{out}} \approx \frac{1}{\sqrt{2}}(\hat{a}_{\text{in}}(f^A) + e^{i\delta}\hat{a}_{\text{in}}(f^B)). \tag{2.60}$$

This can be extended to arbitrary superposition states in the focal plane with nonuniform amplitudes in and relative phases. By using multiple QPAs to synthesize superposition states and interfering them over free space, quantum information protocols for the generation and distribution of entanglement can be constructed for quantum sensing and communication (see Fig. 2.12). In Appendix A, I provide two illustrative examples of QPA protocols for realizing a reconfigurable beamplitter and generating N00N states.

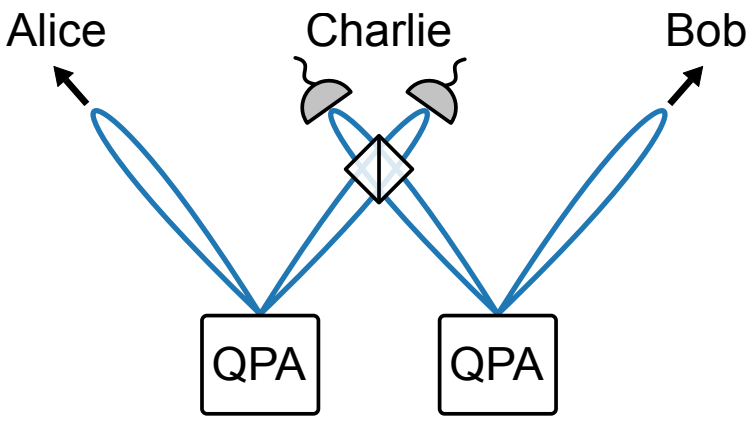

Figure 2.12: Conceptual illustration of quantum communication with multiple QPAs, where photons transmitted to Alice and Bob can be steered by reconfiguring their beams.

QPA receiver system on a chip

In Chapter 6, we used the QRX array discussed in Section 2.6 to realize a phased array system on a chip that can receive, image and manipulate non-classical light over free space. We demonstrate an integrated photonic-electronic system with more than 1000 functional components on-chip to detect squeezed light. By integrating an array of 32 sub-wavelength engineered metamaterial antennas, we demonstrate the first, to our knowledge, direct free-space-to-chip interface for reconfigurable quantum links. On the same chip, we implement the first, to our knowledge, large-scale array of quantum-limited coherent receivers that can resolve non-classical signals simultaneously across 32 channels. With coherent readout and manipulation of these signals, we demonstrate 32-pixel imaging and spatially configurable reception of squeezed light over free space. Our work advances wireless quantum technologies that could enable practical applications in quantum communications and sensing.

References

[1] Robert W. Boyd. Nonlinear Optics. 3rd. San Diego, CA, USA: Academic Press, 2008. ISBN: 978-0123694706.

[2] C.K. Hong and L. Mandel. "Theory of parametric frequency down conversion of light." In: Physical Review A 31.4 (1985), p. 2409.

[3] Bahaa E. A. Saleh and Malvin Carl Teich. Fundamentals of Photonics. 2nd. Hoboken, NJ, USA: Wiley-Interscience, 2007. ISBN: 978-0471358329.

[4] P. G. Kwiat, K. Mattle, H. Weinfurter, A. Zeilinger, A. V. Sergienko, and Y. Shih. "New High-Intensity Source of Polarization-Entangled Photon Pairs."

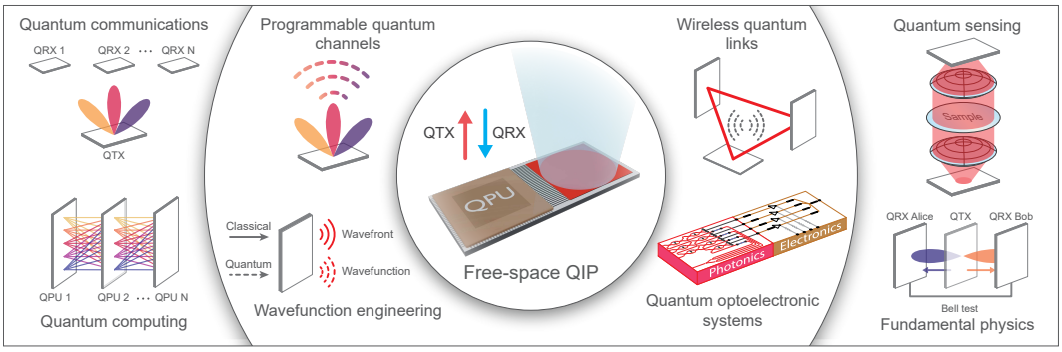

Figure 2.13: Vision for wireless quantum chip technologies with reconfigurable chip-to-free space quantum interconnects enabled by phased array interfaces and their applications in quantum communications, sensing and computing.

In: Physical Review Letters 75.24 (1995), pp. 4337–4341. DOI: 10.1103/PhysRevLett.75.4337.

[5] M. M. Fejer, G. A. Magel, D. H. Jundt, and R. L. Byer. "Quasi-phase-matched second harmonic generation: Tuning and tolerances." In: IEEE Journal of Quantum Electronics 28.11 (1992), pp. 2631–2654. DOI: 10.1109/3.161322.

[6] L. E. Myers, R. C. Eckardt, M. M. Fejer, R. L. Byer, W. R. Bosenberg, and J. W. Pierce. "Quasi-phase-matched optical parametric oscillators in bulk periodically poled LiNbO3." In: Journal of the Optical Society of America B 12.11 (1995), pp. 2102–2116. DOI: 10.1364/JOSAB.12.002102.

[7] Yanhua Shih and C. O. Alley. "New Type of Einstein-Podolsky-Rosen-Bohm Experiment Using Pairs of Light Quanta Produced by Optical Parametric Down Conversion." In: Physical Review Letters 61.26 (1988), pp. 2921–2924. DOI: 10.1103/PhysRevLett.61.2921.

[8] C. K. Hong, Z. Y. Ou, and L. Mandel. "Measurement of Subpicosecond Time Intervals between Two Photons by Interference." In: Physical Review Letters 59.18 (1987), pp. 2044–2046. DOI: 10.1103/PhysRevLett.59.2044.

[9] Wolfgang Tittel, Jürgen Brendel, Hugo Zbinden, and Nicolas Gisin. "Violation of Bell inequalities by photons more than 10 km apart." In: Physical Review Letters 81.17 (1998), p. 3563.

[10] Sébastien Tanzilli, Hugues De Riedmatten, Wolfgang Tittel, Hugo Zbinden, Pascal Baldi, Marc De Micheli, Daniel Barry Ostrowsky, and Nicolas Gisin. "Highly efficient photon-pair source using periodically poled lithium niobate waveguide." In: Electronics Letters 37.1 (2001), pp. 26–28.

[11] Jian-Wei Pan, Zeng-Bing Chen, Chao-Yang Lu, Harald Weinfurter, Anton Zeilinger, and Marek Żukowski. "Multiphoton entanglement and interferometry." In: Reviews of Modern Physics 84.2 (2012), pp. 777–838.

[12] Marco Fiorentino, Sean M Spillane, Raymond G. Beausoleil, Tony D. Roberts, Philip Battle, and Mark W. Munro. “Spontaneous parametric down-conversion in periodically poled KTP waveguides and bulk crystals.” In: Optics Express 15.12 (2007), pp. 7479–7488.

[13] Warren P. Grice and Ian A. Walmsley. “Spectral information and distinguishability in type-II down-conversion with a broadband pump.” In: Physical Review A 56.2 (1997), p. 1627.

[14] Kevin Zielnicki, Karina Garay-Palmett, Daniel Cruz-Delgado, Hector Cruz-Ramirez, Michael F. O’Boyle, Bin Fang, Virginia O. Lorenz, Alfred B U’Ren, and Paul G. Kwiat. “Joint spectral characterization of photon-pair sources.” In: Journal of Modern Optics 65.10 (2018), pp. 1141–1160.

[15] Kevin Zielnicki, Karina Garay-Palmett, Radhika Dirks, Alfred B. U’Ren, and Paul G. Kwiat. “Engineering of near-IR photon pairs to be factorable in space-time and entangled in polarization.” In: Optics Express 23.6 (2015), pp. 7894–7907.

[16] Warren P. Grice, Alfred B. U’Ren, and Ian A. Walmsley. “Eliminating frequency and space-time correlations in multiphoton states.” In: Physical Review A 64.6 (2001), p. 063815.

[17] Alfred B. U’Ren, Konrad Banaszek, and Ian A. Walmsley. “Photon engineering for quantum information processing.” In: arXiv preprint quant-ph/0305192 (2003).

[18] P. J. Mosley, J. S. Lundeen, B. J. Smith, P. Wasylczyk, A. B. U’Ren, C. Silberhorn, and I. A. Walmsley. “Heralded Generation of Ultrafast Single Photons in Pure Quantum States.” In: Physical Review Letters 100.13 (2008). Demonstrates spectral engineering for single–mode operation and reports high heralding efficiency and purity (as indicated by low $g^{(2)}(0)$)., p. 133601.

[19] Luis Edgar Vicent, Alfred B. U’Ren, Radhika Rangarajan, Clara I. Osorio, Juan P. Torres, Lijian Zhang, and Ian A. Walmsley. “Design of bright, fiber-coupled and fully factorable photon pair sources.” In: New Journal of Physics 12.9 (2010), p. 093027.

[20] D. Branning, W.P. Grice, R. Erdmann, and I. A. Walmsley. “Engineering the indistinguishability and entanglement of two photons.” In: Physical Review Letters 83.5 (1999), p. 955.

[21] Thomas Lutz, Piotr Kolenderski, and Thomas Jennewein. “Toward a downconversion source of positively spectrally correlated and decorrelated telecom photon pairs.” In: Optics letters 38.5 (2013), pp. 697–699.

[22] Yasser Jeronimo-Moreno, Saul Rodriguez-Benavides, and Alfred B. U’Ren. “Theory of cavity-enhanced spontaneous parametric downconversion.” In: Laser physics 20 (2010), pp. 1221–1233.

[23] Andrew Mueller, Samantha I. Davis, Boris Korzh, Raju Valivarthi, Andrew D. Beyer, Rahaf Youssef, Neil Sinclair, Cristián Peña, Matthew D Shaw, and Maria Spiropulu. “High-rate multiplexed entanglement source based on time-bin qubits for advanced quantum networks.” In: Optica Quantum 2.2 (2024), pp. 64–71.

[24] Jürgen Brendel, Nicolas Gisin, Wolfgang Tittel, and Hugo Zbinden. "Pulsed energy-time entangled twin-photon source for quantum communication." In: Physical Review Letters 82.12 (1999), p. 2594.

[25] A. Mair, A. Vaziri, G. Weihs, and A. Zeilinger. "Entanglement of the orbital angular momentum states of photons." In: Nature 412 (2001), pp. 313–316. DOI: 10.1038/35085529. URL: https://doi.org/10.1038/35085529.

[26] I. Marcikic, H. de Riedmatten, W. Tittel, V. Scarani, H. Zbinden, and N. Gisin. "Time-bin entangled qubits for quantum communication created by femtosecond pulses." In: Phys. Rev. A 66 (6 Dec. 2002), p. 062308. DOI: 10.1103/PhysRevA.66.062308. URL: https://link.aps.org/doi/10.1103/PhysRevA.66.062308.

[27] Samantha I. Davis, Andrew Mueller, Raju Valivarthi, Nikolai Lauk, Lautaro Narvaez, Boris Korzh, Andrew D. Beyer, Olmo Cerri, Marco Colangelo, Karl K. Berggren, et al. "Improved heralded single-photon source with a photon-number-resolving superconducting nanowire detector." In: Physical Review Applied 18.6 (2022), p. 064007.

[28] Alexander I Lvovsky. "Squeezed light." In: Photonics: Scientific Foundations, Technology and Applications 1 (2015), pp. 121–163.

[29] Hans-A. Bachor and Timothy C. Ralph. A guide to experiments in quantum optics. John Wiley & Sons, 2019.

[30] Christopher C. Gerry and Peter L. Knight. Introductory quantum optics. Cambridge University Press, 2005.

[31] Robert H. Hadfield. "Single-photon detectors for optical quantum information applications." In: Nature photonics 3.12 (2009), pp. 696–705.

[32] Adriana E. Lita, Dileep V. Reddy, Varun B. Verma, Richard P. Mirin, and Sae Woo Nam. "Development of superconducting single-photon and photon-number resolving detectors for quantum applications." In: Journal of Lightwave Technology 40.23 (2022), pp. 7578–7597.

[33] A. J. Miller, S. W. Nam, J. M. Martinis, and A. V. Sergienko. "Demonstration of a low-noise near-infrared photon counter with multiphoton discrimination." In: Applied Physics Letters 83 (2003), pp. 791–793.

[34] A. E. Lita, A. J. Miller, and S. W. Nam. "Counting near-infrared single photons with 95% efficiency." In: Optics Express 16 (2008), pp. 3032–3040.

[35] Brice Calkins, Paolo L. Mennea, Adriana E. Lita, Benjamin J. Metcalf, W. Steven Kolthammer, Antia Lamas-Linares, Justin B. Spring, Peter C. Humphreys, Richard P. Mirin, James C. Gates, et al. "High quantum-efficiency photon-number-resolving detector for photonic on-chip information processing." In: Optics Express 21.19 (2013), pp. 22657–22670.

[36] Georg Harder, Tim J. Bartley, Adriana E. Lita, Sae Woo Nam, Thomas Gerrits, and Christine Silberhorn. "Single-mode parametric-down-conversion states with 50 photons as a source for mesoscopic quantum optics." In: Physical Review Letters 116.14 (2016), p. 143601.

[37] Miller Eaton, Amr Hossameldin, Richard J. Birrittella, Paul M. Alsing, Christopher C. Gerry, Hai Dong, Chris Cuevas, and Olivier Pfister. "Resolution of 100 photons and quantum generation of unbiased random numbers." In: Nature Photonics 17.1 (2023), pp. 106–111.

[38] W. Guo, X. Liu, Y. Wang, Q. Wei, L.F. Wei, J. Hubmayr, J. Fowler, J. Ullom, L. Vale, M.R. Vissers, et al. "Counting near infrared photons with microwave kinetic inductance detectors." In: Applied Physics Letters 110.21 (2017).

[39] P. K. Day, H. G. LeDuc, B. A. Mazin, A. Vayonakis, and J. Zmuidzinas. "A broadband superconducting detector suitable for use in large arrays." In: Nature 425 (2003), pp. 817–821.

[40] Dileep V. Reddy, Robert R. Nerem, Sae Woo Nam, Richard P. Mirin, and Varun B. Verma. "Superconducting nanowire single-photon detectors with 98% system detection efficiency at 1550 nm." In: Optica 7.12 (2020), p. 1649. ISSN: 2334-2536.

[41] Andrew S. Mueller, Boris Korzh, Marcus Runyan, Emma E. Wollman, Andrew D. Beyer, Jason P. Allmaras, Angel E. Velasco, Ioana Craiciu, Bruce Bumble, Ryan M. Briggs, et al. "Free-space coupled superconducting nanowire single-photon detector with low dark counts." In: Optica 8.12 (2021), pp. 1586–1587.

[42] Giovanni V. Resta, Lorenzo Stasi, Matthieu Perrenoud, Sylvain El-Khoury, Tiff Brydges, Rob Thew, Hugo Zbinden, and Félix Bussières. "Gigahertz detection rates and dynamic photon-number resolution with superconducting nanowire arrays." In: Nano Letters 23.13 (2023), pp. 6018–6026.

[43] Boris Korzh, Qing-Yuan Zhao, Jason P. Allmaras, Simone Frasca, Travis M. Autry, Eric A Bersin, Andrew D. Beyer, Ryan M. Briggs, Bruce Bumble, Marco Colangelo, et al. "Demonstration of sub-3 ps temporal resolution with a superconducting nanowire single-photon detector." In: Nature Photonics 14.4 (2020), pp. 250–255.

[44] Andrew J. Kerman, Eric A. Dauler, William E. Keicher, Joel K.W. Yang, Karl K. Berggren, G. Gol'Tsman, and B. Voronov. "Kinetic-inductance-limited reset time of superconducting nanowire photon counters." In: Applied Physics Letters 88.11 (2006).

[45] Di Zhu, Marco Colangelo, Changchen Chen, Boris A. Korzh, Franco N.C. Wong, Matthew D. Shaw, and Karl K. Berggren. "Resolving photon numbers using a superconducting nanowire with impedance-matching taper." In: Nano Letters 20.5 (2020), pp. 3858–3863.

[46] Timon Schapeler, Niklas Lamberty, Thomas Hummel, Fabian Schlue, Michael Stefszky, Benjamin Brecht, Christine Silberhorn, and Tim J. Bartley. "Electrical trace analysis of superconducting nanowire photon-number-resolving detectors." In: Physical Review Applied 22.1 (2024), p. 014024.

[47] Marco Colangelo, Boris Korzh, Jason P. Allmaras, Andrew D. Beyer, Andrew S. Mueller, Ryan M. Briggs, Bruce Bumble, Marcus Runyan, Martin J. Stevens, Adam N. McCaughan, et al. "Impedance-matched differential superconducting nanowire detectors." In: Physical Review Applied 19.4 (2023), p. 044093.

[48] Mamoru Endo, Tatsuki Sonoyama, Mikihisa Matsuyama, Fumiya Okamoto, Shigehito Miki, Masahiro Yabuno, Fumihiro China, Hirotaka Terai, and Akira Furusawa. "Quantum detector tomography of a superconducting nanostrip photon-number-resolving detector." In: Optics Express 29.8 (2021), pp. 11728–11738.

[49] Clinton Cahall, Kathryn L. Nicolich, Nurul T. Islam, Gregory P. Lafyatis, Aaron J. Miller, Daniel J. Gauthier, and Jungsang Kim. "Multi-photon detection using a conventional superconducting nanowire single-photon detector." In: Optica 4.12 (2017), pp. 1534–1535.

[50] Aleksander Divochiy, Francesco Marsili, David Bitauld, Alessandro Gaggero, Roberto Leoni, Francesco Mattioli, Alexander Korneev, Vitaliy Seleznev, Nataliya Kaurova, Olga Minaeva, et al. "Superconducting nanowire photon-number-resolving detector at telecommunication wavelengths." In: Nature Photonics 2.5 (2008), pp. 302–306.

[51] Eric A. Dauler, Andrew J. Kerman, Bryan S. Robinson, Joel K.W. Yang, Boris Voronov, Gregory Goltsman, Scott A. Hamilton, and Karl K. Berggren. "Photon-number-resolution with sub-30-ps timing using multi-element superconducting nanowire single photon detectors." In: Journal of Modern Optics 56.2-3 (2009), pp. 364–373.

[52] Risheng Cheng, Heyu Yin, Jianshe Liu, Tiefu Li, Han Cai, Zheng Xu, and Wei Chen. "Photon-number-resolving detector based on superconducting serial nanowires." In: IEEE Transactions on Applied Superconductivity 23.1 (2012), pp. 2200309–2200309.

[53] Chandra M. Natarajan, Lijian Zhang, Hendrik Coldenstrodt-Ronge, Gaia Donati, Sander N. Dorenbos, Val Zwiller, Ian A. Walmsley, and Robert H. Hadfield. "Quantum detector tomography of a time-multiplexed superconducting nanowire single-photon detector at telecom wavelengths." In: Optics Express 21.1 (2013), pp. 893–902.

[54] Mattias Jönsson, Marcin Swillo, Samuel Gyger, Val Zwiller, and Gunnar Björk. "Temporal array with superconducting nanowire single-photon detectors for photon-number resolution." In: Physical Review A 102.5 (2020), p. 052616.

[55] Ioana Craiciu, Boris Korzh, Andrew D. Beyer, Andrew Mueller, Jason P. Allmaras, Lautaro Narváez, Maria Spiropulu, Bruce Bumble, Thomas Lehner, Emma E. Wollman, et al. "High-speed detection of 1550 nm single photons with superconducting nanowire detectors." In: Optica 10.2 (2023), pp. 183–190.

[56] Lorenzo Stasi, Gaëtan Gras, Riad Berrazouane, Matthieu Perrenoud, Hugo Zbinden, and Félix Bussières. "Fast high-efficiency photon-number-resolving parallel superconducting nanowire single-photon detector." In: Physical Review Applied 19.6 (2023), p. 064041.

[57] Lorenzo Stasi, Towsif Taher, Giovanni V. Resta, Hugo Zbinden, Rob Thew, and Felix Bussieres. “Enhanced detection rate and high photon-number efficiencies with a scalable parallel SNSPD.” In: ACS Photonics 12.1 (2024), pp. 320–329.

[58] Francesco Mattioli, Zili Zhou, Alessandro Gaggero, Rosalinda Gaudio, Roberto Leoni, and Andrea Fiore. “Photon-counting and analog operation of a 24-pixel photon number resolving detector based on superconducting nanowires.” In: Optics Express 24.8 (2016), pp. 9067–9076.

[59] Risheng Cheng, Yiyu Zhou, Sihao Wang, Mohan Shen, Towsif Taher, and Hong X. Tang. “A 100-pixel photon-number-resolving detector unveiling photon statistics.” In: Nature Photonics 17.1 (2023), pp. 112–119.

[60] Frédéric Grosshans, Gilles Van Assche, Jérôme Wenger, Rosa Brouri, Nicolas J. Cerf, and Philippe Grangier. “Quantum key distribution using gaussian-modulated coherent states.” In: Nature 421.6920 (2003), pp. 238–241.

[61] Robert Raussendorf and Hans J. Briegel. “A one-way quantum computer.” In: Physical Review Letters 86.22 (2001), p. 5188.

[62] Robert Raussendorf, Daniel E. Browne, and Hans J. Briegel. “Measurement-based quantum computation on cluster states.” In: Physical review A 68.2 (2003), p. 022312.

[63] D. Ganapathy, W. Jia, M. Nakano, V. Xu, N. Aritomi, T. Cullen, N. Kijbunchoo, S.E. Dwyer, A. Mullavey, L. McCuller, et al. “Broadband quantum enhancement of the LIGO detectors with frequency-dependent squeezing.” In: Physical Review X 13.4 (2023), p. 041021.

[64] Nicolas C. Menicucci, Peter Van Loock, Mile Gu, Christian Weedbrook, Timothy C. Ralph, and Michael A. Nielsen. “Universal quantum computation with continuous-variable cluster states.” In: Physical Review Letters 97.11 (2006), p. 110501.

[65] Daniel Gottesman, Alexei Kitaev, and John Preskill. “Encoding a qubit in an oscillator.” In: Physical Review A 64.1 (2001), p. 012310.

[66] Shuntaro Takeda, Takahiro Mizuta, Maria Fuwa, Peter Van Loock, and Akira Furusawa. “Deterministic quantum teleportation of photonic quantum bits by a hybrid technique.” In: Nature 500.7462 (2013), pp. 315–318.

[67] Axel Schönbeck, Fabian Thies, and Roman Schnabel. “13 dB squeezed vacuum states at 1550 nm from 12 mW external pump power at 775 nm.” In: Optics Letters 43.1 (2017), pp. 110–113.

[68] Han-Sen Zhong, Hui Wang, Yu-Hao Deng, Ming-Cheng Chen, Li-Chao Peng, Yi-Han Luo, Jian Qin, Dian Wu, Xing Ding, Yi Hu, et al. “Quantum computational advantage using photons.” In: Science 370.6523 (2020), pp. 1460–1463.

[69] Galan Moody, Volker J. Sorger, Daniel J. Blumenthal, Paul W. Juodawlkis, William Loh, Cheryl Sorace-Agaskar, Alex E. Jones, Krishna C. Balram, Jonathan C. F. Matthews, Anthony Laing, et al. “2022 Roadmap on integrated quantum photonics.” In: Journal of Physics: Photonics 4.1 (2022), p. 012501.

[70] Jianwei Wang, Fabio Sciarrino, Anthony Laing, and Mark G. Thompson. “Integrated photonic quantum technologies.” In: Nature Photonics 14.5 (2020), pp. 273–284.

[71] Graham T. Reed. “Silicon photonics: the state of the art.” In: (2008).

[72] Di Zhu, Linbo Shao, Mengjie Yu, Rebecca Cheng, Boris Desiatov, C. J. Xin, Yaowen Hu, Jeffrey Holzgrafe, Soumya Ghosh, Amirhassan Shams-Ansari, et al. “Integrated photonics on thin-film lithium niobate.” In: Advances in Optics and Photonics 13.2 (2021), pp. 242–352.

[73] Lukas Chrostowski and Michael Hochberg. Silicon photonics design: from devices to systems. Cambridge University Press, 2015.

[74] H. Aghaee Rad, T. Ainsworth, R. N. Alexander, B. Altieri, M. F. Askarani, R. Baby, L. Banchi, B. Q. Baragiola, J.E. Bourassa, R. S. Chadwick, et al. “Scaling and networking a modular photonic quantum computer.” In: Nature (2025), pp. 1–8.

[75] Jie Sun, Erman Timurdogan, Ami Yaacobi, Zhan Su, Ehsan Shah Hosseini, David B. Cole, and Michael R. Watts. “Large-scale silicon photonic circuits for optical phased arrays.” In: IEEE Journal of Selected Topics in Quantum Electronics 20.4 (2013), pp. 264–278.

[76] Christopher Rogers, Alexander Y. Piggott, David J. Thomson, et al. “A universal 3D imaging sensor on a silicon photonics platform.” In: Nature 590.7845 (Feb. 2021), pp. 256–261.

[77] Volkan Gurses, Samantha I. Davis, Esme Knabe, Raju Valivarthi, Maria Spiropulu, and Ali Hajimiri. “A compact silicon photonic quantum coherent receiver with deterministic phase control.” In: CLEO: Applications and Technology. Optica Publishing Group. 2023, AM4N–4.

[78] Volkan Gurses, Debjit Sarkar, Samantha Davis, and Ali Hajimiri. “An integrated photonic-electronic quantum coherent receiver for sub-shot-noise-limited optical links.” In: Optical Fiber Communication Conference. Optica Publishing Group. 2024, Tu2C–1.

[79] Mirko Pittaluga, Yuen San Lo, Adam Brzosko, Robert I. Woodward, Davide Scalcon, Matthew S. Winnel, Thomas Roger, James F. Dynes, Kim A. Owen, Sergio Juárez, et al. “Long-distance coherent quantum communications in deployed telecom networks.” In: Nature 640.8060 (2025), pp. 911–917.

[80] Alexander I Lvovsky and Michael G Raymer. “Continuous-variable optical quantum-state tomography.” In: Reviews of Modern Physics 81.1 (2009), p. 299.

[81] Behzad Razavi. Design of Integrated Circuits for Optical Communications. 2nd ed. Wiley, 2012.

[82] Alfred B. U’Ren, Christine Silberhorn, Konrad Banaszek, and Ian A. Walmsley. “Efficient conditional preparation of high-fidelity single photon states for fiber-optic quantum networks.” In: Physical Review Letters 93.9 (2004), p. 093601.

[83] Sylvain Fasel, Olivier Alibart, Sebastien Tanzilli, Pascal Baldi, Alexios Beveratos, Nicolas Gisin, and Hugo Zbinden. “High-quality asynchronous heralded single-photon source at telecom wavelength.” In: New Journal of Physics 6.1 (2004), p. 163.

[84] Andreas Eckstein, Andreas Christ, Peter J. Mosley, and Christine Silberhorn. “Highly efficient single-pass source of pulsed single-mode twin beams of light.” In: Physical Review Letters 106.1 (2011), p. 013603.

[85] Amideddin Mataji-Kojouri and Marco Liscidini. “Narrow-band photon pair generation through cavity-enhanced spontaneous parametric down-conversion.” In: Physical Review A 108.5 (2023), p. 053714.

[86] Andreas Christ and Christine Silberhorn. “Limits on the deterministic creation of pure single-photon states using parametric down-conversion.” In: Physical Review A 85.2 (2012), p. 023829.

[87] Reinhard F. Werner. “Quantum states with Einstein-Podolsky-Rosen correlations admitting a hidden-variable model.” In: Physical Review A 40.8 (1989), p. 4277.

[88] John F. Clauser, Michael A. Horne, Abner Shimony, and Richard A. Holt. “Proposed experiment to test local hidden-variable theories.” In: Physical Review Letters 23.15 (1969), p. 880.

[89] Antonio Acín, Nicolas Brunner, Nicolas Gisin, Serge Massar, Stefano Pironio, and Valerio Scarani. “Device-independent security of quantum cryptography against collective attacks.” In: Physical Review Letters 98.23 (2007), p. 230501.

[90] Joel F. Tasker, Jonathan Frazer, Giacomo Ferranti, and Jonathan C. F. Matthews. “A Bi-CMOS electronic photonic integrated circuit quantum light detector.” In: Science Advances 10.20 (2024), eadk6890.

[91] Yoann Piétri, Luis Trigo Vidarte, Matteo Schiavon, Laurent Vivien, Philippe Grangier, Amine Rhouni, and Eleni Diamanti. “Experimental demonstration of Continuous-Variable Quantum Key Distribution with a silicon photonics integrated receiver.” In: Optica Quantum 2.6 (2024), pp. 428–437.

[92] Cédric Bruynsteen, Michael Vanhoecke, Johan Bauwelinck, and Xin Yin. “Integrated balanced homodyne photonic–electronic detector for beyond 20-GHz shot-noise-limited measurements.” In: Optica 8.9 (Sept. 2021), pp. 1146–1152.

[93] G. Zhang, J. Y. Haw, H. Cai, et al. “An integrated silicon photonic chip platform for continuous-variable quantum key distribution.” In: Nature Photonics 13.12 (Dec. 2019), pp. 839–842.

[94] Yongqiang Du, Xin Hua, Zhengeng Zhao, Xiaoran Sun, Zhenrong Zhang, Xi Xiao, and Kejin Wei. “Source-independent quantum random number generators with integrated silicon photonics.” In: Communications Physics 8.1 (2025), p. 9.

[95] Cédric Bruynsteen, Tobias Gehring, Cosmo Lupo, Johan Bauwelinck, and Xin Yin. “100-Gbit/s integrated quantum random number generator based on vacuum fluctuations.” In: PRX quantum 4.1 (2023), p. 010330.

[96] Tommaso Bertapelle, Marco Avesani, Alberto Santamato, Alberto Montanaro, Marco Chiesa, Davide Rotta, Massimo Artiglia, Vito Sorianello, Francesco Testa, Gabriele De Angelis, et al. "High-speed source-device-independent quantum random number generator on a chip." In: Optica Quantum 3.1 (2025), pp. 111–118.

[97] A. I. Lvovsky and M. G. Raymer. "Continuous-variable optical quantum-state tomography." In: Rev. Mod. Phys. 81 (1 Mar. 2009), pp. 299–332.

[98] Jürgen Appel, Dallas Hoffman, Eden Figueroa, and A. I. Lvovsky. "Electronic noise in optical homodyne tomography." In: Physical Review A 75.3 (2007), p. 035802.

[99] Carmen Porto, Davide Rusca, Simone Cialdi, Andrea Crespi, Roberto Osellame, Dario Tamascelli, Stefano Olivares, and Matteo G.A. Paris. "Detection of squeezed light with glass-integrated technology embedded into a homodyne detector setup." In: Journal of the Optical Society of America B 35.7 (2018), pp. 1596–1602.

[100] Joel F. Tasker, Jonathan Frazer, Giacomo Ferranti, Euan J. Allen, Léandre F. Brunel, Sébastien Tanzilli, Virginia D'Auria, and Jonathan C. F. Matthews. "Silicon photonics interfaced with integrated electronics for 9 GHz measurement of squeezed light." In: Nature Photonics 15.1 (Jan. 2021), pp. 11–15.

[101] Stefano Pirandola. "Limits and security of free-space quantum communications." In: Physical Review Research 3.1 (2021), p. 013279.

[102] Andrej Kržič, Sakshi Sharma, Christopher Spiess, Uday Chandrashekara, Sebastian Töpfer, Gregor Sauer, Luis Javier González-Martín del Campo, Teresa Kopf, Stefan Petscharnig, Thomas Grafenauer, et al. "Towards metropolitan free-space quantum networks." In: npj Quantum Information 9.1 (2023), p. 95.

[103] Sheng-Kai Liao, Wen-Qi Cai, Wei-Yue Liu, Liang Zhang, Yang Li, Ji-Gang Ren, Juan Yin, Qi Shen, Yuan Cao, Zheng-Ping Li, et al. "Satellite-to-ground quantum key distribution." In: Nature 549.7670 (2017), pp. 43–47.

[104] Ji-Gang Ren, Ping Xu, Hai-Lin Yong, Liang Zhang, Sheng-Kai Liao, Juan Yin, Wei-Yue Liu, Wen-Qi Cai, Meng Yang, Li Li, et al. "Ground-to-satellite quantum teleportation." In: Nature 549.7670 (2017), pp. 70–73.

[105] Robert C. Hansen. Phased array antennas. John Wiley & Sons, 2009.

[106] Aobo Li, Shreya Singh, and Dan Sievenpiper. "Metasurfaces and their applications." In: Nanophotonics 7.6 (2018), pp. 989–1011.

[107] Barry D. Van Veen and Kevin M. Buckley. "Beamforming: A versatile approach to spatial filtering." In: IEEE ASSP Magazine 5.2 (1988), pp. 4–24.

[108] Constantine A. Balanis. Antenna theory: analysis and design. John wiley & sons, 2016.